Journal of Photochemistry & Photobiology, A: Chemistry 466 (2025) 116387

Contents lists available at ScienceDirect

Journal of Photochemistry & Photobiology, A: Chemistry

journal homepage: www.elsevier.com/locate/jphotochem

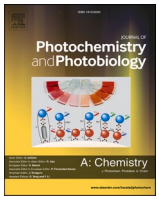

GO and CNT template impact on the WO_3/Bi_2S_3 photocatalytic activity for pharmaceutical active compounds removal

Alexandru Enesca

Pro ro ro r r r o r o r o o

ARTICLE INFO

or
Antibiotics
Carbon nanotubes
Graphene oxide
Photocatalysis
Wastewater

ABSTRACT

A combined sol–gel and doctor blade techniques were used to obtain two types of composites. Graphene oxide (GO) and carbon nanotubes (CNTs) were used as template in the sol–gel procedure which include two steps: WO_3 and Bi_2S_3 development. The composites crystallinity and morphology were investigated indicating the formation of monoclinic WO_3 and orthorhombic Bi_2S_3. The GO template samples exhibit porous sponge-like morphology with 285 m^2/g S_{BET}, while the CNTs template samples have a granular morphology with 294 m^2/g S_{BET}. The elemental analysis indicate that the composite components are evenly distributed through the sample. Both GO and CNTs based samples have a predominant polar component of the surface energy which make them suitable candidate for applications in aqueous environments. The photocatalytic removal efficiency was tested in the presence penicillin G and amoxicillin (150 ppm) under UV and Vis irradiation. The highest efficiencies correspond to $GO/WO_3/Bi_2S_3$ which was able to remove 57.43 % PEN-G and 63.94 % AMO. The photocatalytic mechanism was investigated and described in details.

1. Introduction

The presence of pharmaceutic active compounds in wastewater have significantly increase in the last 10 years, and even more after the COVID crisis. Recent studies indicate an increase with 70 % in the hospital wastewater and 30 % in the householder's wastewater [1–3]. Permissive legislation in some countries as well as excessive preventive medication contributed to this trend. The wastewater treatment plants faced difficulties to address these problems using traditional methods [4,5]. Photocatalysis represent a real alternative to overcome this problem, having the advantage of using light radiation and reduce quantities of photocatalytic materials in order to remove organic pollutants [6,7].

Graphene oxide (GO) and carbon nanotubes (CNTs) have been used in photocatalytic application due to their adsorbent and conductive capacities [8–10]. Photocatalysis is a two-step procedure based on simultaneous adsorption and oxidation processes [11,12]. The use of large active surface materials can have an important impact on the photocatalytic efficiency [13]. Coupling these materials with metal-based semiconductors create a synergic effect that can enhance the oxidative species photogeneration acting on the organic pollutant mineralization. The photoactivity of graphene oxide (GO) coupled with GO/MgO [14], GO/Bi_2WO_6 [15], GO/TiO_2 [16,17], GO/Cu_xSnSO [18], GO/Fe_3O_4 [19], GO/CeO_2 [20], GO/Co_3O_4 [21], GO/ZnO [22] and GO/CuO [23] was evaluated for organic pollutant degradation. Mahanna and co. [14] reported 85.1 % degradation of reactive blue 222 (RB-222) dye after 120 min of irradiation. Carbon nanotubes (CNTs) were coupled with CNTs/ZnO [24], $CNTs/BiVO_4$ [25], $CNTs/TiO_2$ [26,27], $CNTs/ZnIn_2S_4$ [28], $CNTs/CuCo_2O_4/Co_3S_4$ [29], $CNTs/LaFeO_3$ [30], $CNTs/SnO_2$ [31], $CNTs/WO_3$ [32] and $CNTs/Co_3O_4$ [33]. Warsi and co. [30] reported 81.65 % degradation efficiency toward crystal violet dye after 140 min of irradiation with visible light. These materials benefit from an extended absorption spectrum (both UV and Vis), increased conductivity (due to GO and CNTs insertion) and high charge carriers photogeneration (due to the presence of metal-based semiconductor). However, the major disadvantage consist of fast recombination charge and reduced chemical stability at certain pH values.

The present paper proposes a simple and efficient method to develop tandem structures based on WO_3 and Bi_2S_3 using GO and CNTs as growing templates. This method allows the formation of uniform composite particles with large surface area. Due to the doublet structure, the charge carrier recombination is reduced and the electrical mobility increases. The presence of crystalline structure, sample morphology and topography are discussed. Based on the photocatalytic mechanism corresponding to each composite, the removal of penicillin G (PEN-G) and amoxicillin (AMO) in the presence of UV and Vis radiation is described in details.

r aenesca@unitbv.ro.

https://doi.org/10.1016/j.jphotochem.2025.116387
Received 9 October 2024; Received in revised form 16 February 2025; Accepted 10 March 2025
Available online 17 March 2025

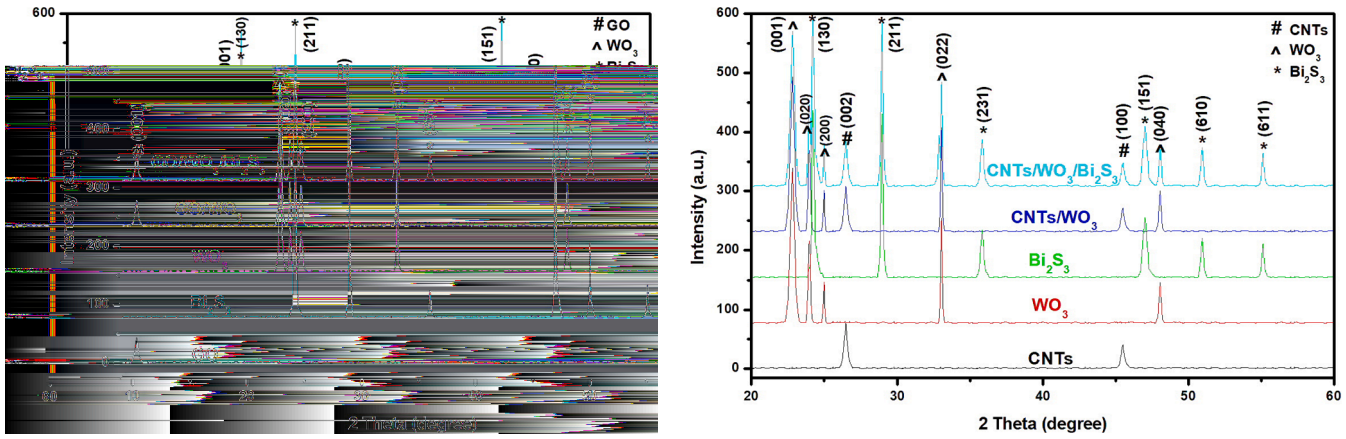

Fig. 1. Diffraction patterns corresponding to (a) GO series and (b) CNTs series.

Table 1
Films physical parameters and components crystalline sizes.

Samples	Thickness [μm]*	Volume [cm^3]	Weight [g]	Density [g/cm^3]	S_{BET} (m^2/g)	Crystallite size (Å)	
						WO_3	Bi_2S_3
GO/WO_3	1.94	1.21×10^{-3}	3.93×10^{-3}	3.25	242	77.2	–
$GO/WO_3/Bi_2S_3$	2.18	1.36×10^{-3}	4.71×10^{-3}	3.47	285	–	127.9
CNT/WO_3	1.87	1.16×10^{-3}	3.66×10^{-3}	3.16	268	83.6	–
$CNT/WO_3/Bi_2S_3$	2.13	1.33×10^{-3}	4.51×10^{-3}	3.39	294	–	136.3

*Calculated from the reflectance spectra at 6° incident angle.

2. Materials and methods

Po r

ro r r o r

The composite heterostructure was developed following a two-step sol–gel method:

(i) GO/WO_3 and $CNTs/WO_3$ synthesis: 0.6 mol for tungsten hexachloride ($WCl_6 \cdot 2H_2O$, 99.8 %, Honeywell, Berlin, Germany) was dissolved in alcoholic mixture of *o*-propanol (100 %, C_3H_7OH, Merck, Darmstadt, Germany) and absolute methanol (CH_3OH, Merck, Darmstadt, Germany). Previously, 0.1 % of GO and CNTs were separately dispersed into the alcoholic solution to serve as crystallization support for WO_3. 1 N sodium hydroxide (99.8 %, Merck, Darmstadt, Germany) was slowly added under the magnetic stirring until the gel was formed. The pH value was maintained around 11.5 to avoid gel dissolution, considering that NaOH behave as a reducing agent without anions stabilization. The maturation period was 24 h in dark and the yellow product was centrifuged and annealed at 430 °C for 6 h.

(ii) $GO/WO_3/Bi_2S_3$ and $CNTs/WO_3/Bi_2S_3$ synthesis: 0.4 mol bismuth nitrate ($Bi(NO_3)_3 \cdot 5H_2O$, 98.9 %, Sigma Aldrich, Munich, Germany) was dissolved in deionized water. Previously, the GO/WO_3 and $CNTs/WO_3$ were separately dispersed in the deionized water to serve as support for Bi_2S_3 development. 0.6 mol of sodium thiosulfate ($Na_2S_2O_3$, 99.3 %, Merck, Darmstadt, Germany) was added under continuous stirring until the gel was formed. Maturation was done for 14 h in dark at room temperature and a gray powder was collected after centrifugation. The powder was thermally treated into a hermetic ceramic capsule containing rich sulfur atmosphere at 135 °C.

ro r r

or o

The film was obtained by doctor blade procedure using a thick paste containing $GO/WO_3/Bi_2S_3$ or $CNTs/WO_3/Bi_2S_3$, absolute ethanol (C_2H_5OH, Merck, Darmstadt, Germany) and triton x-100 (Sigma Aldrich, Munich, Germany) serving as nonionic surfactant additive to increase the film adhesion on the substrate surface. Pieces of 2.5 cm × 2.5 cm of microscopic glass were used as substrate after rigorous cleaning in ultrasound bath with ethanol and acetone. The paste was dispersed on the substrate surface with a raclette at a constant rate of 1.2 s/cm. The film was thermally treated in open air at 110 °C for 5 h.

P o o r

During the photocatalytic experiments 3 sources of UV (Philips black tube with 18 W, 320–360 nm, $\lambda_{max} = 340$ nm) and 5 sources of Vis (Philips cold tune with 18 W, 390–720 nm, $\lambda_{max} = 570$ nm) with a total 12.75 mW/cm^2 irradiance. The temperature was maintained constant at 22 °C during the irradiation using ventilation engine and humidity stabilizers. Two 150 ppm solutions were prepared by dissolving penicillin G (PEN-G, Apollo Scientific, Bredbury, UK) and amoxicillin (AMO, Apollo Scientific, Bredbury, UK) in ultrapure water. One piece of microscopic glass covered with $GO/WO_3/Bi_2S_3$ or $CNTs/WO_3/Bi_2S_3$ was inserted in quartz glasses containing 40 mL of PEN-G or AMO. Before starting the irradiation, the solutions were preserved for 2 h in dark to reach the adsorption–desorption equilibrium. Finally, the samples were exposed for 10 h to UV–Vis irradiation and the photocatalytic activity was hourly evaluated.

r r o

The presence of crystalline structure was analyzed using a MiniFlex 600 diffractometer (XRD, Rigaku, Tokyo, Japan) and the surface elemental composition was evaluated by energy dispersive X-ray method (EDS 7, ThermoScientific, Waltham, MA, USA). The XRD diffraction parameters were: 2 theta between 20 and 60°, 0.03 degree

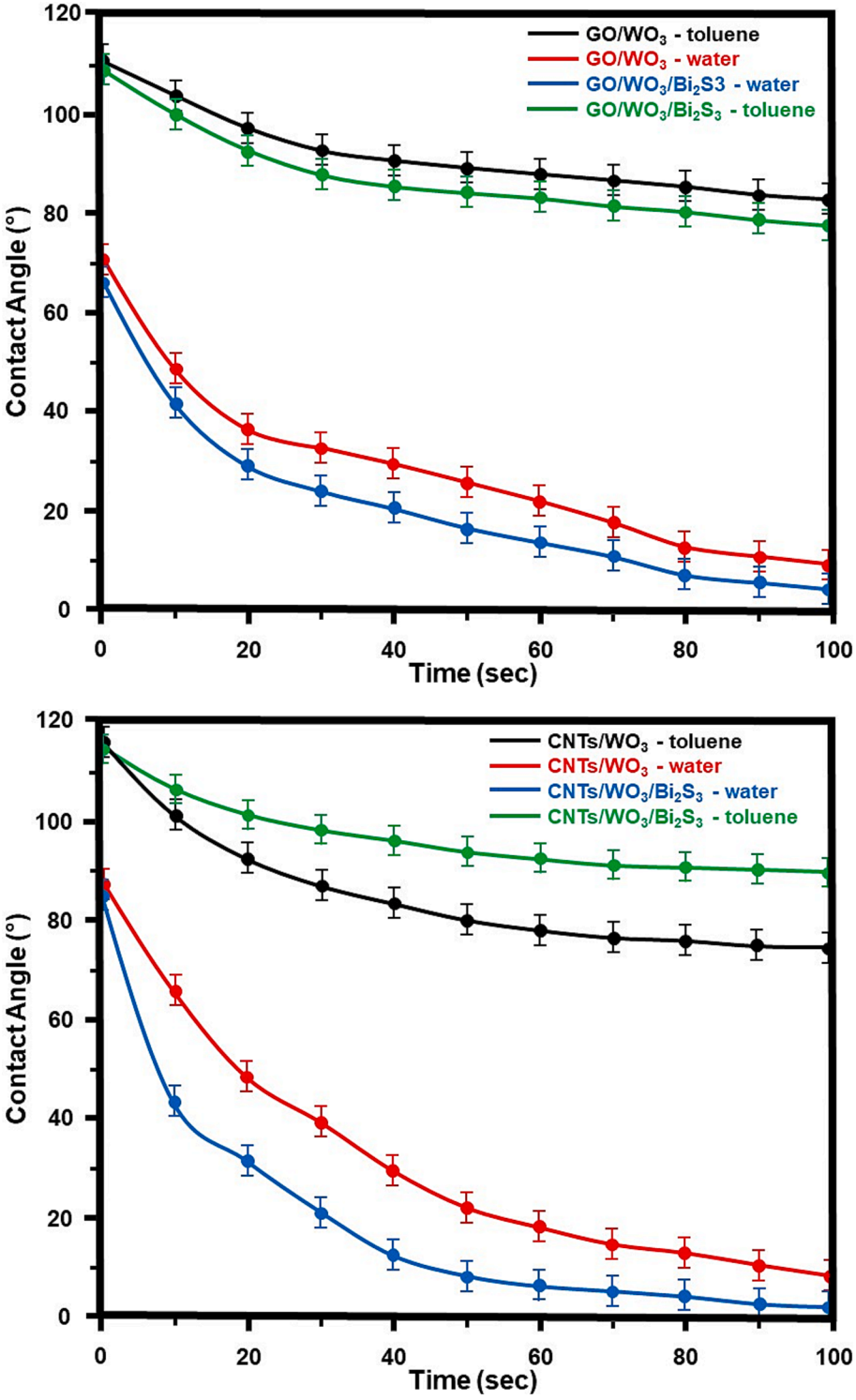

Fig. 2. Contact angle measurements with polar and non-polar liquids (a) GO series and (b) CNTs series.

Table 2
Evaluation of the polar and dispersive surface energy components.

Samples code	Surface energy σ [mN/m]	Dispersive component σ^d [mN/m]	Polar component σ^p [mN/m]
GO/WO_3	99.8	16.3	83.5
$GO/WO_3/Bi_2S_3$	110.3	18.6	91.7
CNT/WO_3	101.5	25.1	76.4
$CNT/WO_3/Bi_2S_3$	111.0	28.2	82.8

steps and a rate of 0.05 s/step. The surface evaluation was done in order to determine: (i) the main component of the surface energy (OCA-20 ContactAngle-meter, DataPhysics Instruments), (ii) morphology (FESEM, SU8010, Fukuoka, Japan) and topography (SPM, Digital Instruments Inc., USA). The SEM investigation was done at 10 kV accelerated voltage, and the AFM images were collected in semi-contact typing procedure using 0.15 N/m force constant and 20 nm tip radius. The optical properties were evaluated with a UV–Vis spectrometer (Lambda950, Perkin Elmer, Waltham, MA, USA) and the specific active

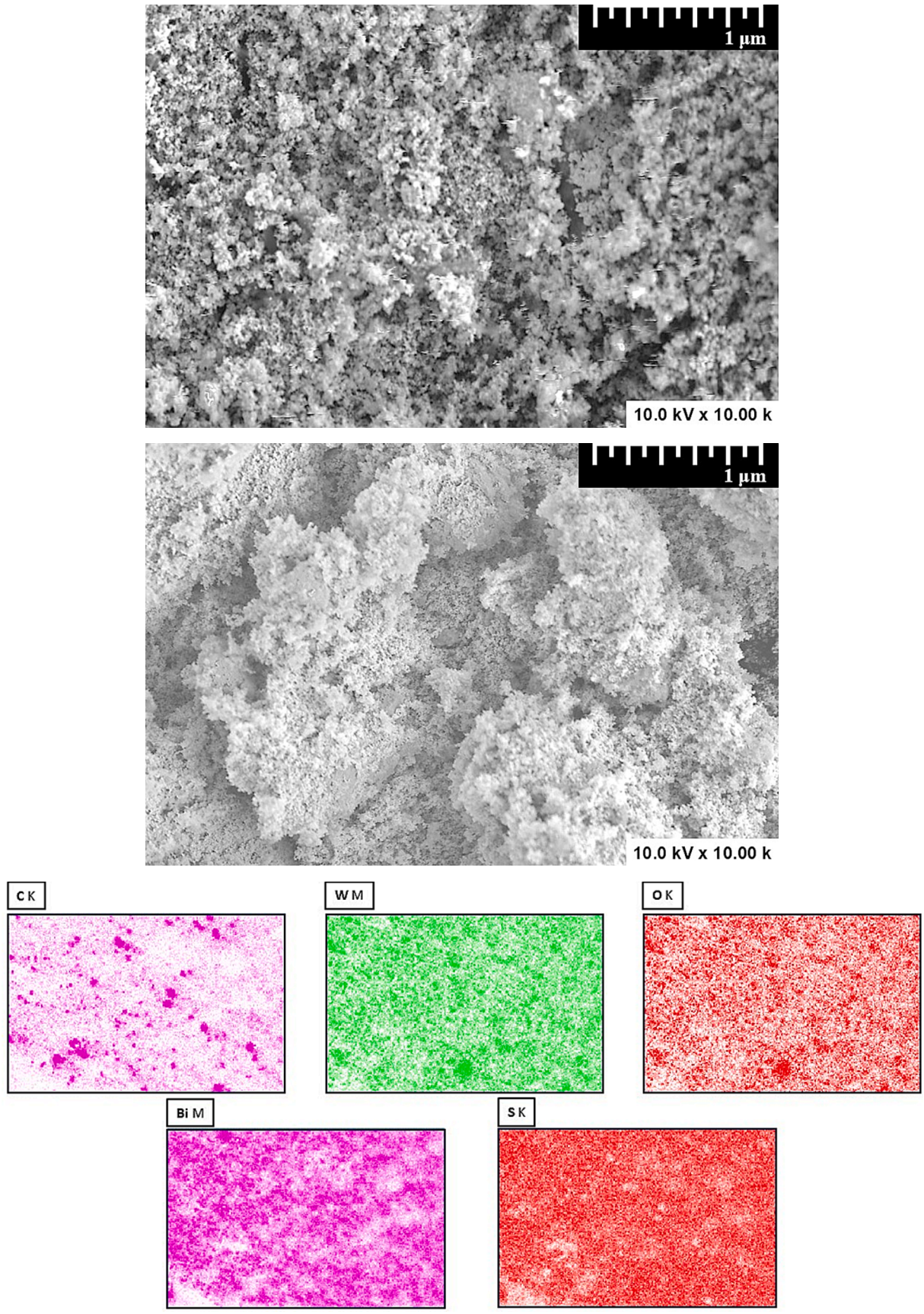

Fig. 3. SEM images of (a) GO/WO_3, (b) GO/WO_3/Bi_2S_3 and (c) EDX corresponding to GO/WO_3/Bi_2S_3.

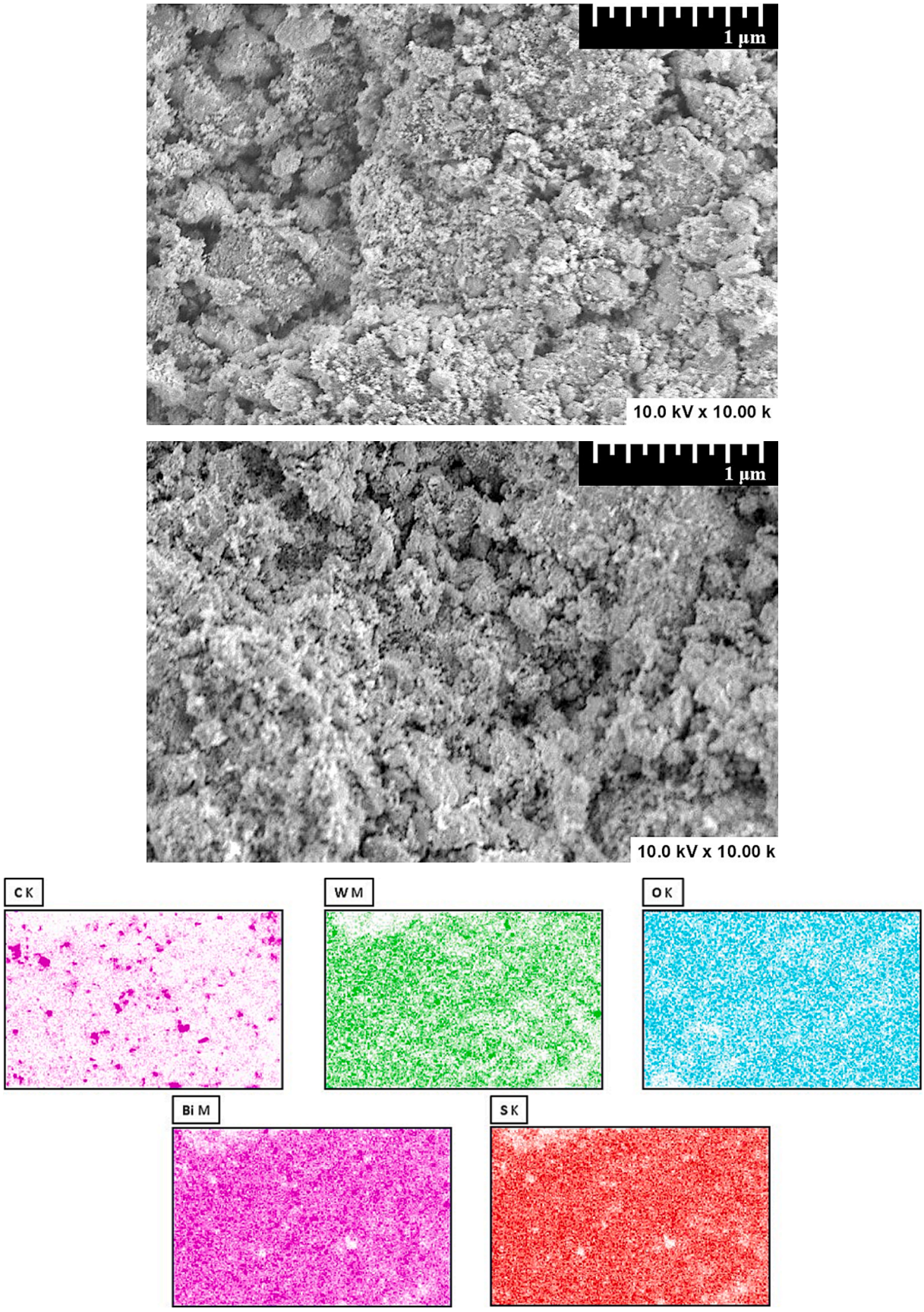

Fig. 4. SEM images of (a) CNTs/WO_3, (b) CNTs/WO_3/Bi_2S_3 and (c) EDX corresponding to CNTs/WO_3/Bi_2S_3.

Table 3
Photocatalysts elemental composition.

Components	Elemental composition [% at]						
	W	O	O_{th}*	Bi	S	S_{th}*	C
$GO/WO_3/Bi_2S_3$	12.9	32.7	51.7	18.9	26.2	28.3	9.3
$CNTs/WO_3/Bi_2S_3$	13.5	28.1	40.5	19.6	28.7	29.4	10.1

* Theoretic content calculated based on the stoichiometry.

surface was measured with a porosimeter (Tristar II Plus Model, Micromeritics, GA, USA).

The photocatalytic investigation was done using two complementary procedures: spectrometric measurements at specific wavelength (221 nm for PEN-G and 270 nm for AMO) and total organic carbon/total nitrogen evaluation (TOC-L and TNM-L, model CPN, Shimadzu, Kyoto, Japan).

The mineralization by-products were investigated by gas chromatography coupled with mass spectroscopy (GC–MS) for PEN-G and high-performance liquid chromatography (HPLC) for AMO. The GC–MS was done with Agilent using an Inferno™ column (Phenomenex 30 m × 0.25 m × 0.25 m) and the HPLC was equipped with a UV detector for 240 nm wavelength and 10 μL injection volume. The transformation products were detected using Q2 time-of-flight mass spectrometer (Bruker).

The electrochemical impedance spectroscopy (EIS) evaluation was done with a ZENNIUM electrochemical workstation, using different frequency ranges and 10 mV modulation signal. The measurements were performed at room temperature using Pt wire as counter-electrode and Ag/AgCl as reference electrode.

3. Results and discussions

o o o or o o

Diffraction investigations presented in Fig. 1 indicate the formation of monoclinic WO_3 structure (JCPDS 83-0951) after the first synthesis step on both GO and CNTs templates. The WO_3 crystallite sizes (see Table 1) were smaller on GO template (77.2 Å) compared with CNTs template (83.6 Å). The crystallite size depends on the high energy state surface points present on GO and CNTs which act as nucleation sources for the WO_3 development [34]. On the second synthesis step Bi_2S_3 is formed and exhibit orthorhombic structure (JCPDS 84-279). The same tendency was observed for Bi_2S_3 crystallite sizes which are smaller (127.9 Å) when deposed on WO_3/GO compared with WO_3/CNTs (136.3 Å).

Methodology used for crystallite size evaluation was based on Scherrer relation (Eq. (1)) where the Braggs angle in represented by θ, Röntgen radiation ($CuK_\alpha 1$, 1.5406 Å) is λ and the angular width value of the peak evaluated at the half maximum intensity (FWHM) is symbolized by β [35].

$$= \frac{0.9\lambda}{\beta\ o\ \theta}, \tag{1}$$

The crystallization of the second component (Bi_2S_3) occur mostly on the WO_3 which cover the template surface (GO or CNTs). However, direct Bi_2S_3 crystallization on uncovered template surface can't be excluded. These analyses don't give any indication of sulfur diffusion in the lower layer or oxygen diffusion in the upper layer. The presence residual components formed during the synthesis process may be possible but was not outlined by the X-ray diffraction.

Table 1 include the film physical parameters and shows that the samples exhibit rather thick layers, with a thickness increasing from around 1.9 μm when WO_3 is deposed up to 2.1 μm when Bi_2S_3 is added. An important parameter for photocatalytic applications is represented by the specific active surface [36]. One reason for choosing GO and CNTs as template was the advantage of using their large surfaces as nucleation sites for the semiconductor components [37,38]. While pristine GO and CNTs have a specific active surface of 136 m^2/g and 189 m^2/g respectively, the nitrogen adsorption–desorption isotherm indicates an increase of the S_{BET} value with the addition of each component as follows: from 242 m^2/g (GO/WO_3) to 285 m^2/g ($GO/WO_3/Bi_2S_3$) and from 268 m^2/g ($CNTs/WO_3$) to 294 m^2/g ($CNTs/WO_3/Bi_2S_3$). High active surface values are beneficial for the photocatalytic activity which is an interface dependent process that induce simultaneously the pollutant adsorption and oxidation [39].

Another important parameter for evaluating the suitability of using this samples in photocatalytic applications is represented by the surface energy [40,41]. Contact angle measurements were done with two liquids with different polarity as presented in Fig. 2. The two liquids were: (1) toluene as non-polar molecule with 28.5 mN/m dispersive component and 0 mN/m polar component and (2) water as polar molecule with 26.25 mN/m dispersive component and 46.55 mN/m polar component. Based on these records the dispersive and polar components of the samples surface energy were calculated using the Fowkes relation (Eq. (2)) and the results are presented in Table 2.

$$\sigma\ \ (1+\ o\ \theta) = 2\left[\left(\sigma\ \ \sigma\ \ \right)^{1/2} + \left(\sigma\ \ \sigma\ \ \right)^{1/2}\right], \tag{2}$$

where the dispersive and polar components of the solid and liquid – surface energies are represented by σ , σ , σ and σ [42].

Fig. 2 indicate an accelerated decrease of the contact angle for both sample series when water was used as testing liquid. Additionally, the surface energy evaluation indicates the polar component as predominant part in the overall values. The GO series exhibit polar components of 83.5 mN/m for GO/WO_3 and 91.7 mN/m for $GO/WO_3/Bi_2S_3$. The polar components corresponding to CNTs series are 76.4 mN/m for $CNTs/WO_3$ and 82.8 mN/m for $CNTs/WO_3/Bi_2S_3$ samples. Increased surface energy can be considered as an indicator of increased hydrophilicity which is a relevant characteristic when aqueous working conditions are used. Additionally, the polar component contribution of the surface energy indicates the hydrophilic photocatalysts behavior. Establishing a good interface between the photocatalysts and the aqueous solutions will facilitate oxidation reactions that take place during the mineralization. Except composition, the template influence seems to play an important role in the wettability properties. Even if $CNTs/WO_3$ have a higher surface energy which is an indicator of good surface wettability, the polar component of the energy is larger for GO/WO_3. Consequently, by coupling WO_3 with GO the surface polarity increases which make these materials suitable candidates for applications in aqueous solutions. However, the differences between GO/WO_3 and $CNTs/WO_3$ are marginal and both materials exhibit good wettability properties. It was concluded that the GO and CNT series exhibit a hydrophilic behavior and can be used as photocatalysts in aqueous environments.

The samples morphology and quantitative analysis was investigated by SEM and EDX. Fig. 3(a) and (b) shows the GO/WO_3 and $GO/WO_3/Bi_2S_3$ morphologies. Both samples exhibit porous sponge-like morphologies which favor the formation of large specific surface areas. After adding the Bi_2S_3 component the sample look more denser which was confirmed by the physical parameter's evaluation presented in Table 1. The morphology is uniform through the surface which indicate that the WO_3 and Bi_2S_3 were evenly distributed. These results are confirmed by EDX evaluation presented in Fig. 3(c) which shows a homogenous distribution of the main composite components, excepting carbon which is partially screened by the WO_3 and Bi_2S_3 developed on the GO template [43]. When changing from GO to CNTs template the morphology presented in Fig. 4(a) and (b) is characterized by the presence of granular structures with various sizes unevenly distributed through the surface. The EDX analysis (Fig. 4(c)) indicate the presence of non-uniformities in the carbon distribution and relative similar density of the other elements. There are no indicators of aggregates development which may consist on different compositions and structures.

The elemental composition obtained from EDX analysis was compared with the theoretical values calculated based on the stoichiometric content that constitute the composite structure, and the results are presented in Table 3. It is worth mentioning that EDX have limitation in terms of layer penetration and the results should be considered as indicative [44,45]. The results show a significant oxygen deficit which may be caused by the diffusion process during the annealing treatment [46]. Additionally, a small sulfur deficit was recorded even if the synthesis and thermal treatment was done in sulfur rich atmosphere. The ions diffusion (O^{2-} and S^{2-}) through the interstices is not uncommon an have been reported in other paper as well [47]. The process in described by the solid-state Eqs. (3) and (4), and is considered as an important source of free radical formation that can enhance the photocatalytic activity.

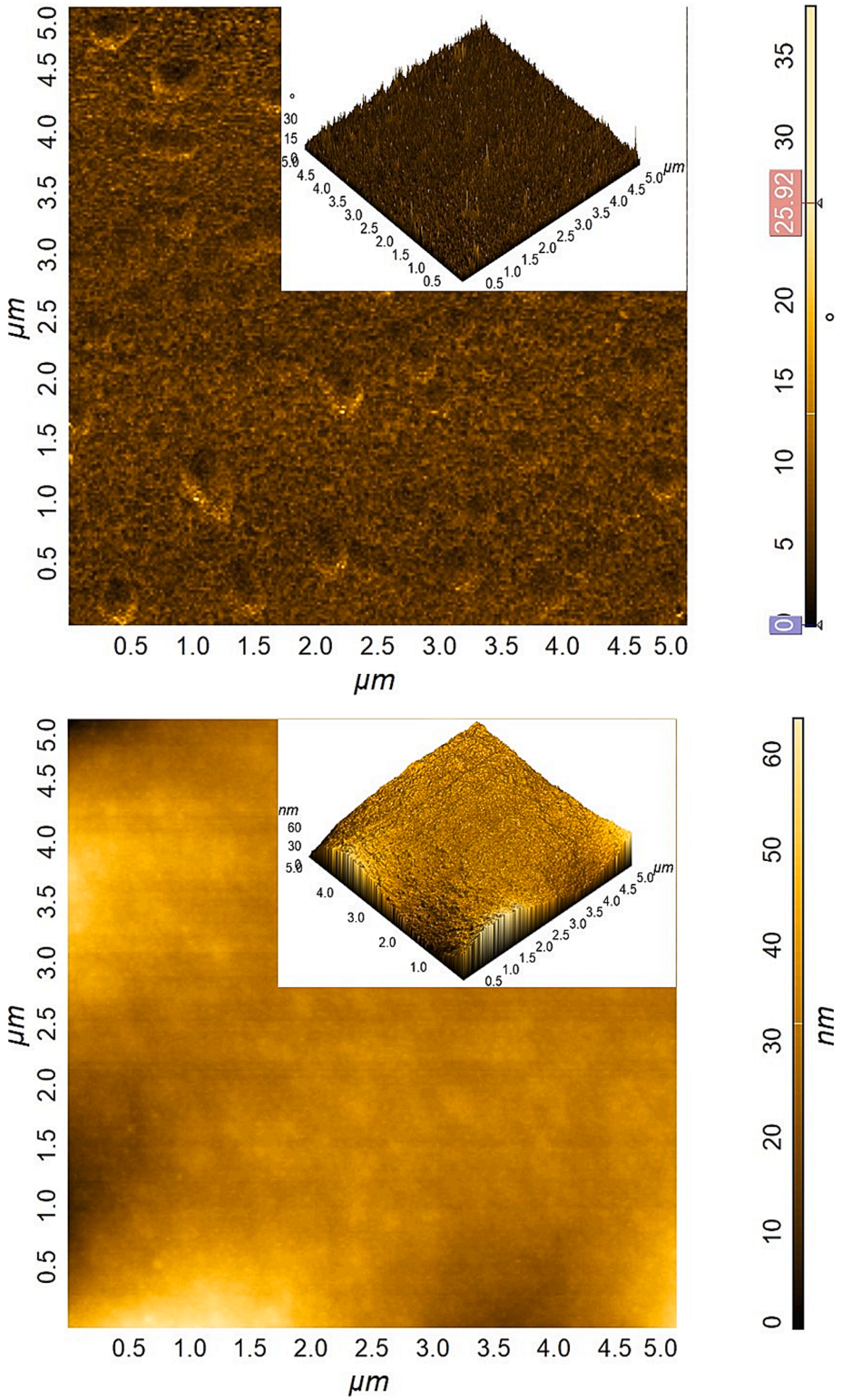

Fig. 5. AFM images of (a) GO/WO_3, (b) GO/WO_3/Bi_2S_3, (c) CNTs/WO_3 and (d) CNTs/WO_3/Bi_2S_3.

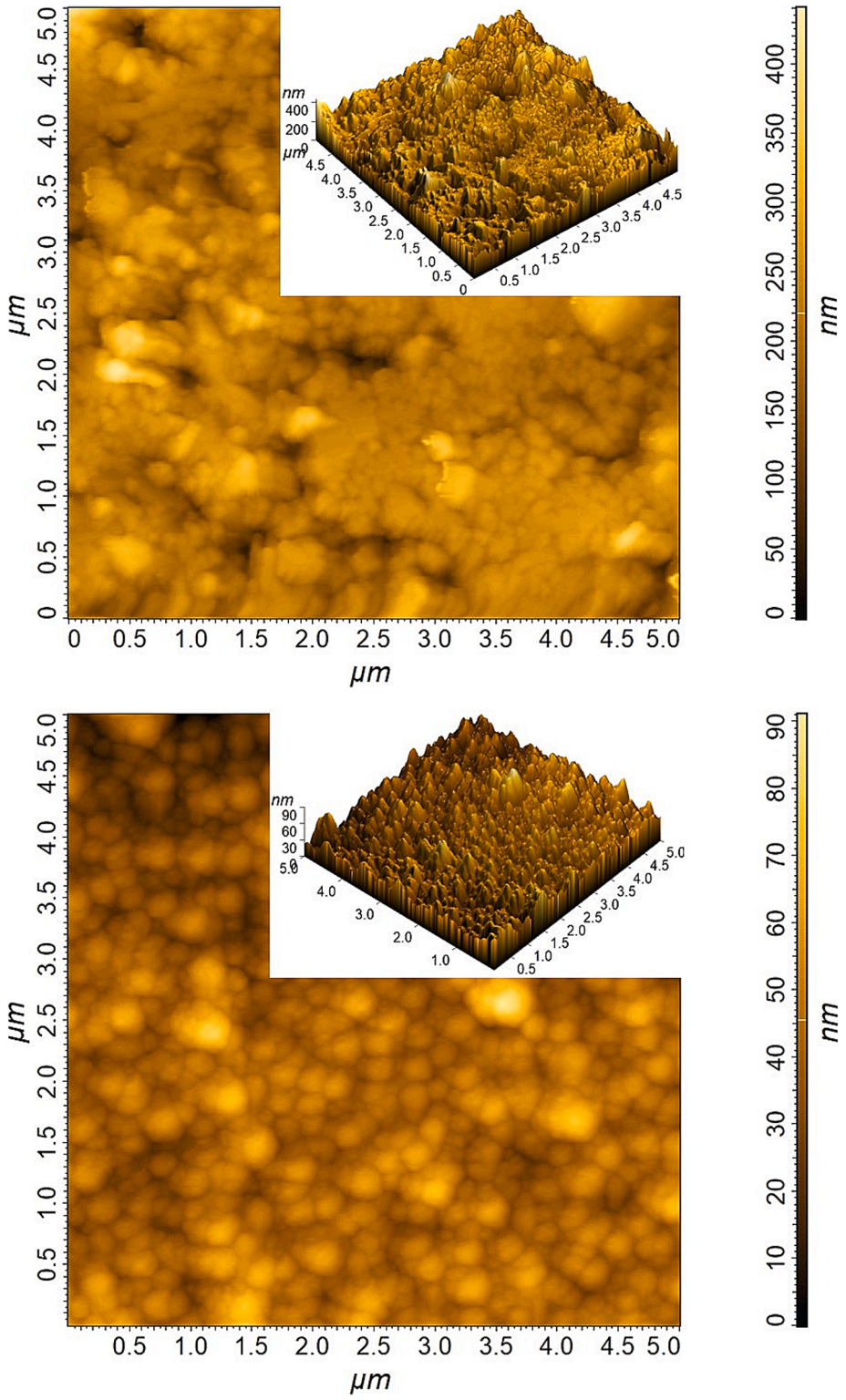

Fig. 5. (*o*).

$$\rightarrow {}^{2+} + {}^{2-}, \quad (3)$$

$$\rightarrow {}^{2+} + {}^{2-}, \quad (4)$$

Interchange ions insertion (Eqs. (5) and (6)) in vacancies may be possible during the diffusion process and can generate a hole's drift current through the heterostructure [48].

$$^{2+} + {}^{2-} \rightarrow \quad + 2\ {}^{+}, \quad (5)$$

$$^{2+} + {}^{2-} \rightarrow \quad + 2\ {}^{+}, \quad (6)$$

The AFM analysis presented in Fig. 5 were done in order to investigate the samples topography. The evaluation was made in semi-contact mode with a tip radius of 20 nm. The morphological differences between GO

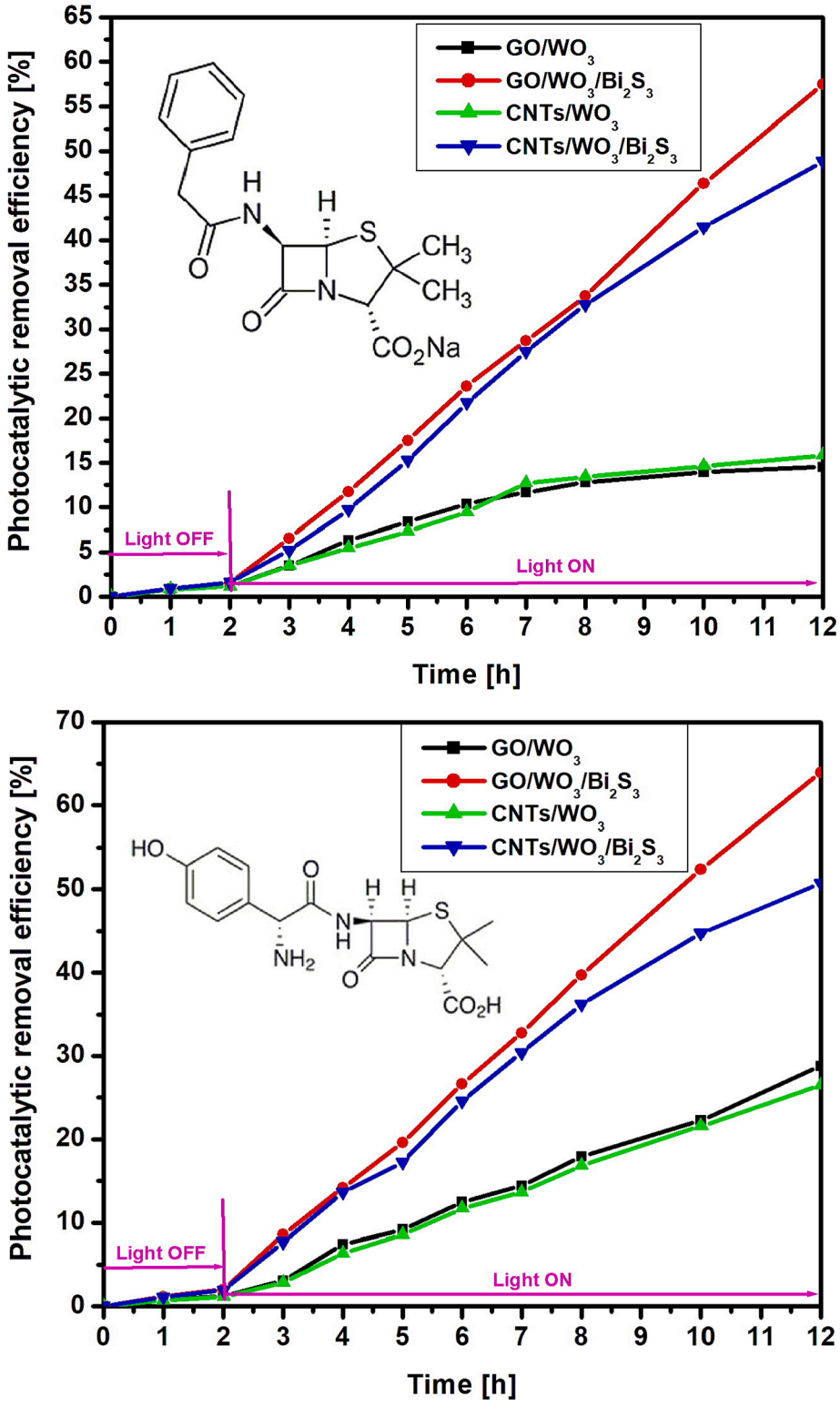

Fig. 6. Photocatalytic activity of the samples toward (a) penicillin G (PEN-G) and (b) amoxicillin (AMO).

and CNTs series become more obvious with this procedure and confirm the results obtained from SEM. The grain shape can be clearly observed only for the CNTs series, and is predominant for the CNTs/WO_3/Bi_2S_3 sample. The CNTs/WO_3 contain smaller and condensed grains. GO based samples are characterised by uniform surface without significant defects such as holes or fractures. The RMS values are larger for CNTs samples (≈ 250 for CNTs/WO_3 and ≈ 100 for CNTs/WO_3/Bi_2S_3) compared with GO samples (≈ 30 for GO/WO_3 and ≈ 50 for GO/WO_3/Bi_2S_3).

P o o

The photocatalytic removal efficiency toward penicillin G (PEN-G) and amoxicillin (AMO) was tested in the presence of UV–Vis irradiation.

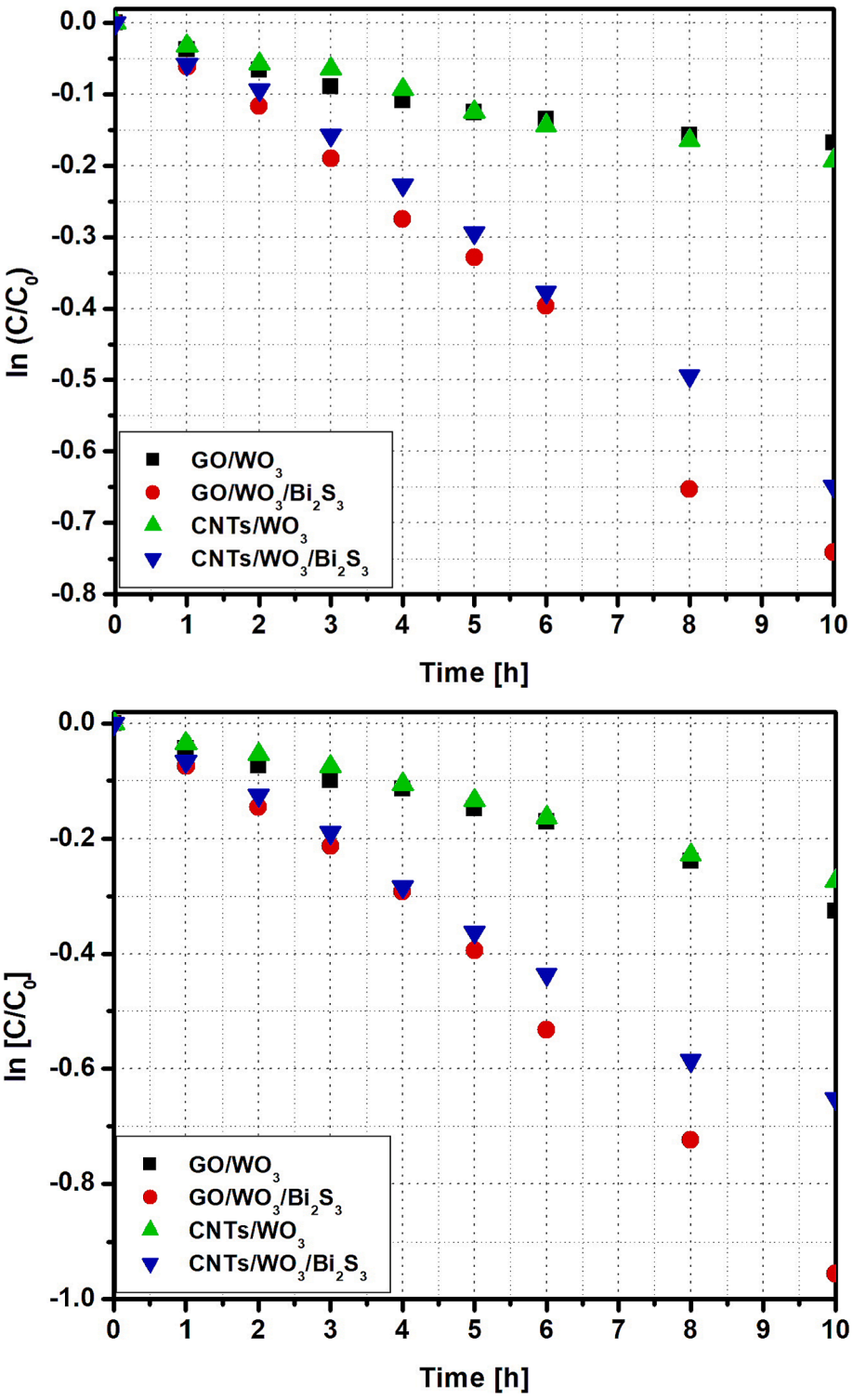

Fig. 7. Kinetic evaluation of the photocatalytic activity towards (a) PEN-G and (b) AMO.

Table 4
Kinetic parameters corresponding to GO and CNT series.

Samples	PEN-G		AMO	
	k (s^{-1})	R^2	k (s^{-1})	R^2
GO/WO_3	0.0138	0.973	0.0315	0.997
$GO/WO_3/Bi_2S_3$	0.0795	0.996	0.0978	0.994
CNT/WO_3	0.031	0.994	0.0311	0.996
$CNT/WO_3/Bi_2S_3$	0.072	0.997	0.0746	0.998

Using spectrometric analysis, the maximum absorbance peak corresponding to each pollutant (221 nm for PEN-G and 270 nm for AMO) was hourly measured and compared with the calibration curve. Based on those measurements the removal efficiency was calculated using Eq. (7) where C_0 is the initial concentration and C is the current concentration [49].

$$\eta = \frac{^{0}-}{^{0}}\ 100, \tag{7}$$

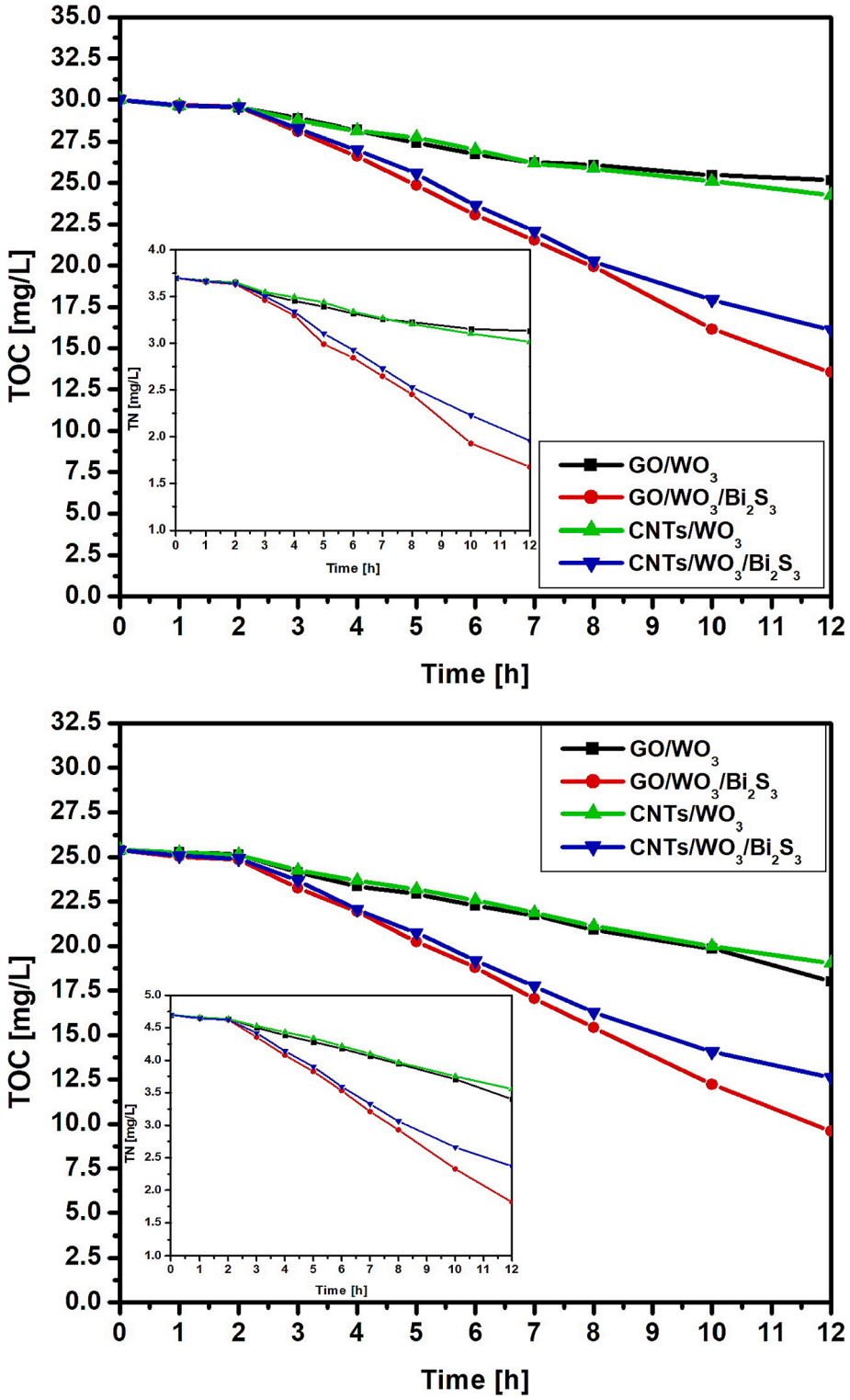

Fig. 8. Total organic carbon (inset Total Nitrogen) removal toward (a) PEN-G and (b) AMO.

The photocatalytic PEN-G removal (Fig. 6a) shows that the samples composed on template/WO_3 exhibit after 10 h of irradiation only 14.53 % (GO/WO_3) and 15.82 % ($CNTs/WO_3$) efficiency. However, by adding Bi_2S_3 on GO/WO_3 and $CNTs/WO_3$ the photoactive heterostructure is able to increase the concentration of photogenerated charge carriers and the formation of (super)oxidative species. As a result, the removal efficiency increases up to 57.43 % for $GO/WO_3/Bi_2S_3$ and 48.83 % for $CNTs/WO_3/Bi_2S_3$. A similar behavior was observed for AMO removal (Fig. 6b) were GO/WO_3 and $CNTs/WO_3$ shows 28.78 % and 26.47 % respectively. The Bi_2S_3 insertion will increase the removal efficiency to 63.94 % for $GO/WO_3/Bi_2S_3$ and 50.69 % for $CNTs/WO_3/Bi_2S_3$. It must be noticed that the samples based on GO template have a slightly higher efficiency compared with CNTs samples, due to the larger polar component of the surface energy which increase the hydrophilicity [50].

The kinetic evaluation of the photocatalytic removal efficiency was included in Fig. 7 and Table 4. Langmuir-Hinshelwood model based on

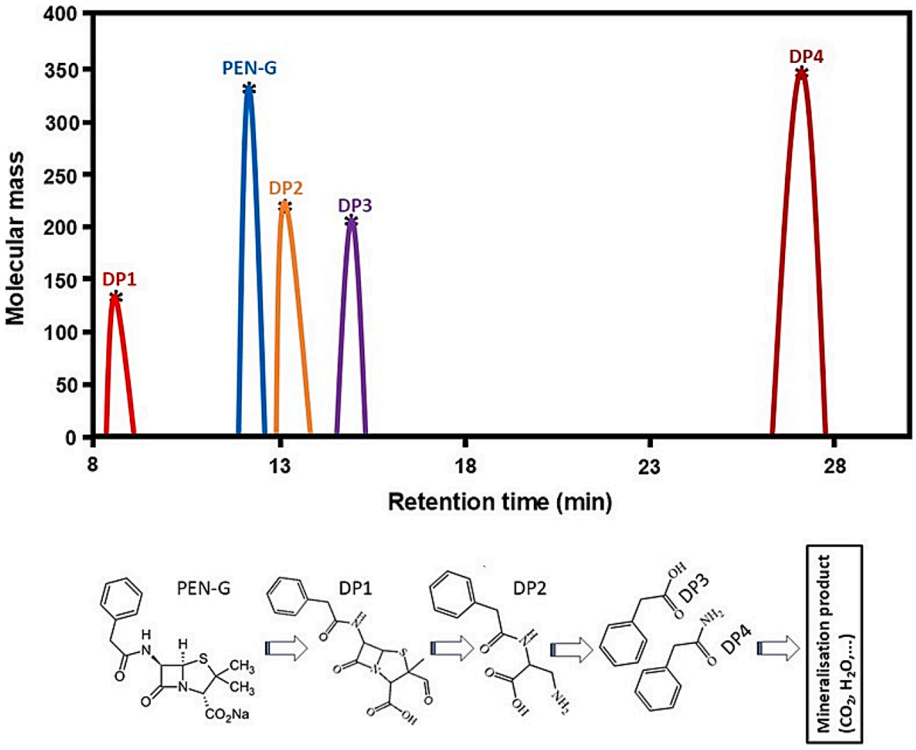

Fig. 9. PEN-G degradation molecules investigated by GC–MS.

Eq. (8) was find to well fit the photocatalytic trend during the 10 h of irradiation. C_0 and C have the same significance as in Eq. (8), k is the rate constant and t is time [51].

$$\ln \quad = \ln \ _0 - \tag{8}$$

The results indicate a significant increase of the rate constant, up to 5.7 for PEN-G removal when GO/WO_3 is replaced with $GO/WO_3/Bi_2S_3$ and 2.3 when $CNTs/WO_3$ is replaced with $CNTs/WO_3/Bi_2S_3$. The evaluation done on AMO removal indicate 3.1 higher rate constant for $GO/WO_3/Bi_2S_3$ compared with GO/WO_3. When $CNTs/WO_3/Bi_2S_3$ is used the constant rate is 2.4 higher than that of $CNTs/WO_3$. These results indicate that the heterostructure development during the second synthesis step play a significant role on enhancing the photocatalytic activity during the UV–Vis irradiation [52].

Considering that spectrometric method is not enough to prove the pollutant mineralization, as the molecules can be partially decomposed, TOC and TN measurement were made and are presented in Fig. 8. The results obtained from TOC evaluation indicate small differences compared with the data obtained from spectrometric measurements. For example, the TOC removal efficiency for PEN-G corresponding to $GO/WO_3/Bi_2S_3$ is 54.89 %, with around 2.5 % difference comparing with the spectrometric evaluation. A similar difference (2.2 %) was observed when the data for $CNTs/WO_3/Bi_2S_3$ toward PEN-G were compared. The results fit even better for AMO removal where the TOC removal efficiency was 62.21 % for $GO/WO_3/Bi_2S_3$ and 50.33 % for $CNTs/WO_3/Bi_2S_3$. In this case the differences where 1.73 % for $GO/WO_3/Bi_2S_3$ and 0.36 % for $CNTs/WO_3/Bi_2S_3$. Similar values obtained from two different evaluation methods indicate that the percentages correspond predominantly to the pollutant mineralization [53,54].

The mineralized products obtained during the PEN-G photocatalytic degradation were evaluated by GC–MS and the results are presented in Fig. 9. The results indicate 12 min retention time for PEN-G and the formation of 4 by-products. The degradation process starts with UV–Vis sensitive β-lactam ring which induce the hydrolytic de-activation of the antibiotic activity. It must be noticed that the major part of the PEN-G (51.39) is completely mineralized and around 2.5 % is converted in other by-products, while 45.11 % of PEN-G remain in solution after 10 h of irradiation.

The AMO degradation products were investigated by HPLC and the UPLC spectrum indicate five retention peaks with the corresponding mass spectra presented in Fig. 10. Excepting AMO, four by-products were detected indicating the presence of a hydrolytic pathway which begin at nitrogen atoms lone electron pair which are the most susceptible to hydroxyl radicals' activity. The reaction chain is presented in Fig. 10 which show the formation of mineralization products without β-lactam ring and the oxidation of methyl groups from thiazolidine ring.

Three pH values (3, 6.5 and 9) were use to investigate the photocatalytic activity of $GO/WO_3/Bi_2S_3$ and $CNTs/WO_3/Bi_2S_3$ samples (see Fig. 11). The results indicate that the highest photocatalytic efficiency is obtained at pH 6.5 which indicate that at this pH value there are the most favorable electrostatic attraction between AMO/PEN-G molecules and heterostructures surface active sites. When pH value decreases at 3 or increases at 9 the photocatalytic activity is drastically reduced. At low pH values (e.g. 3) both antibiotics and heterostructures are positively charged which induce repulsion forces between them, leading to the decrease of the photocatalytic activity. Similar, at high pH values (e.g. 9) the participants are positively charged and repulsion forces occurs. These results are consistent with other studies [55–57] indicating the favorable pH value is between 5.5 and 6.8.

The photocatalytic mechanism was further investigated in order to better understand the processes occurring during the PEN-G and AMO removal. The band gap of each component (Fig. 12a and b) was determined from spectrometric evaluation corroborated with Tauc plot and the results are in agreement with our previous work [58]. PL spectra presented in Fig. 12c was used according with the method described by Sheibani [59] obtained with Varian Cary Eclipse Fluorescence spectrophotometer and was used to confirm the Eg values in the composite samples. Additionally, the energy band values were calculated using the

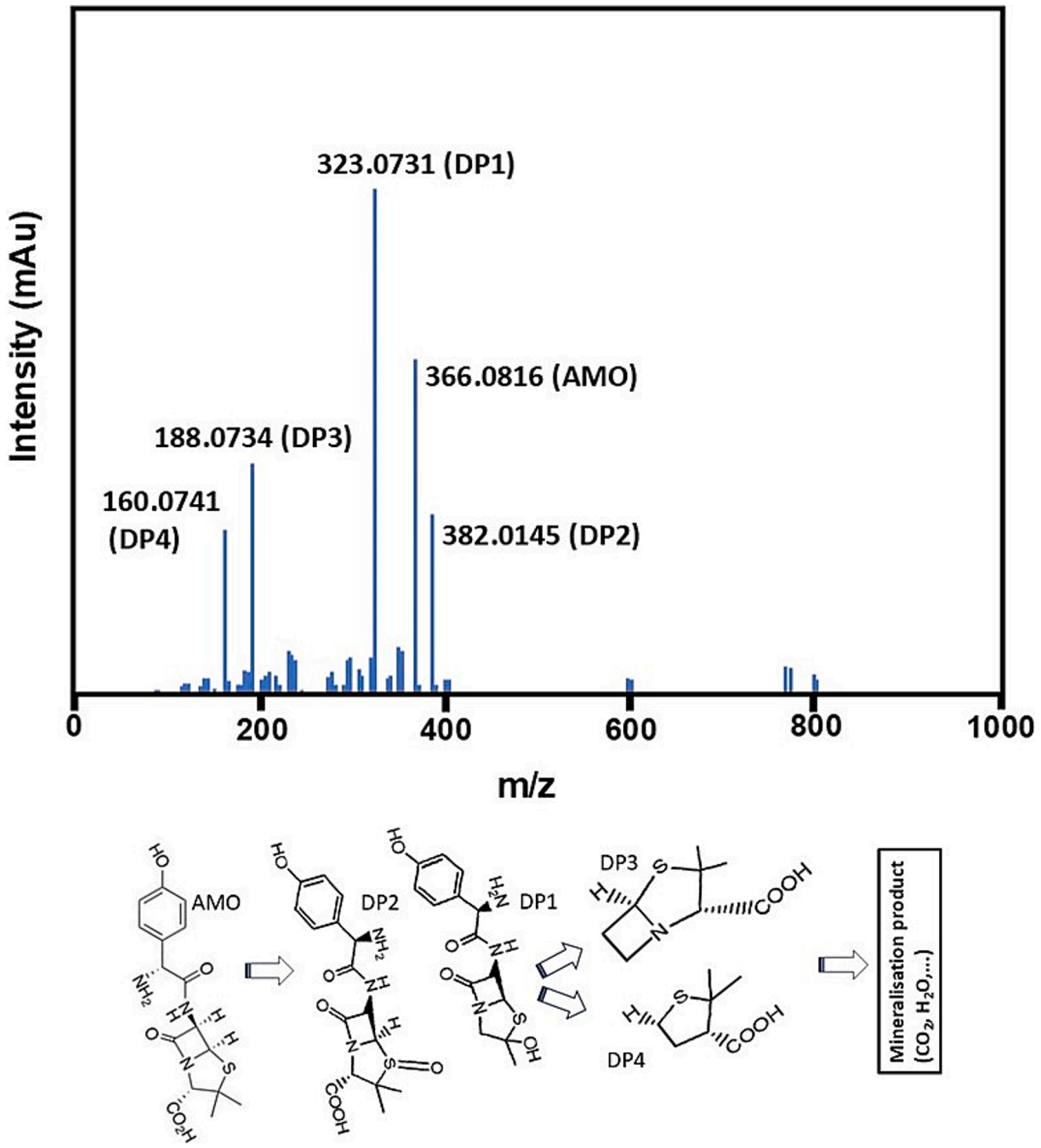

Fig. 10. AMO degradation molecules investigated by HPLC.

methodology described by Mise [60] and Gao [61] which integrate the free electron energy vs. hydrogen E_e, specific cationic electronegativity in Pauling units χ_{cation} (P.u.), absolute cationic electronegativity χ_{cation} (eV) with semiconductor electronegativity $\chi_{semiconductor}$ (eV) and the corresponding band gap E_G value in the following Eqs. (9)–(12):

$$= \chi \quad _o \quad _{or} - \quad + 0.5 \quad , \tag{9}$$

$$= \quad - \quad , \tag{10}$$

$$\chi \quad _o \quad _{or}(\quad) = 0.45 \times \chi \quad _o (\quad) + 3.36, \tag{11}$$

$$\chi \quad _o (\quad) = \frac{\chi \quad _o (P. \ .) + 0.206}{0.336}, \tag{12}$$

The band energy diagrams presented in Fig. 12d and e follows the photogenerated charge carriers' mobility pathway based on the band energy position vs. NHE (eV). According to Eqs. (13) and (14) the charge carriers are generated during the light irradiation.

$$_{2 \ 3} \xrightarrow{\nu} \ ^-(\quad _{2 \ 3}) + \ ^+(\quad _{2 \ 3}), \tag{13}$$

$$_3 \xrightarrow{\nu} \ ^-(\quad _3) + \ ^+(\quad _3), \tag{14}$$

The mechanism describes the transfer of photogenerated electrons from the Bi_2S_3 conduction band (−0.05 eV) to WO_3 conduction band (+0.52 eV). Both energy band are below the $O_2/{}^{\bullet}O_2^-$ potential (−0.33 eV) [62] which makes it difficult to use these radicals during the PEN-G and AMO removal when CNTs template is involved. However, GO template provide additional potential due to the conduction band value of −0.52 eV which is enough to produce superoxidative species as described in Eq. (15). This explains why the samples developed on GO template exhibits higher photocatalytic activity.

$$^-(\quad / \quad _{2 \ 3} + \quad _{2 \ 3}/ \quad _3) + \quad _2 \rightarrow \bullet \quad _2^-, \tag{15}$$

The photogenerated holes migrate from the tungsten oxide valence band (+3.65 eV) to Bi_2S_3 valence band (+1.65 eV) in the CNTs/WO_3/Bi_2S_3 sample. When GO is used as template an intermediary energy level (+2.59 eV) act as buffer for the hole transition. In both cases (CNTs and GO template) the potential required for oxidative radical production of +1.99 eV ($^{\bullet}OH/HO^-$) is available in accordance with Eq. (16).

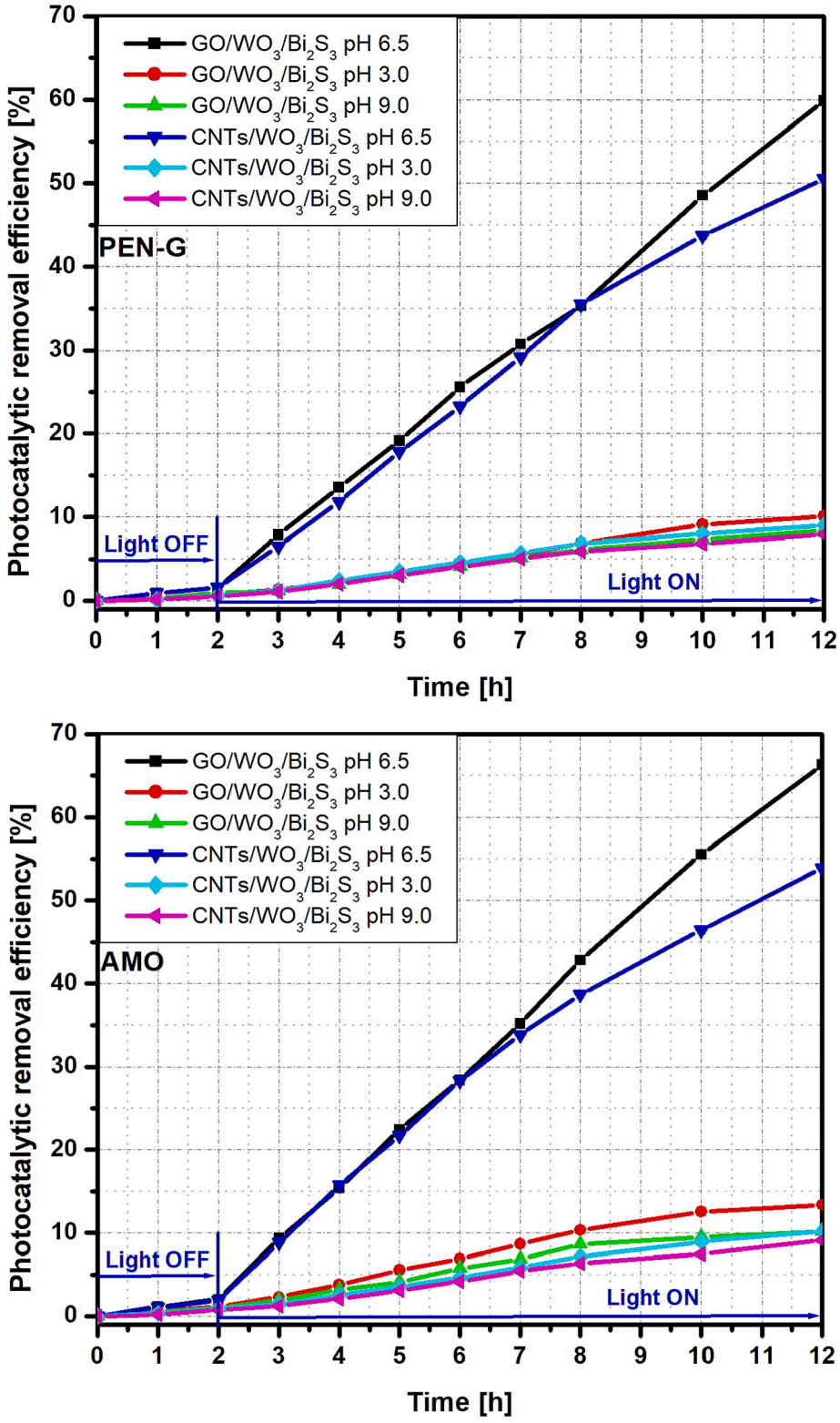

Fig. 11. The pH influence on (a) PEN-G photocatalytic removal and (b) AMO photocatalytic removal.

$$^{-}(\quad {}_{3}/\quad {}_{2\,3}) + \quad {}_{2} \rightarrow \bullet \quad + \quad ^{+}, \tag{16}$$

Electrochemical impedance spectroscopy (EIS) studies were used to determine the electrochemical conductivity of the photocatalytic materials. As presented in Fig. 13 the smallest arc radius of the EIS Nyquist curve corresponds to $GO/WO_3/Bi_2S_3$ and $CNTs/WO_3/Bi_2S_3$ samples which confirms that these heterostructures have lover impedance and high photogenerated charge carriers separation due to the synergy between the metal semiconductors and carbon based templates. The arc radius increases for the bi-component samples (GO/WO_3 and $CNTs/WO_3$) and the largest values correspond to the bare templates (GO and CNTs). There results indicate that the charges recombination is higher for GO and CNTs and decreases by adding metals semiconductors components. Similar results were reported in other papers [63]

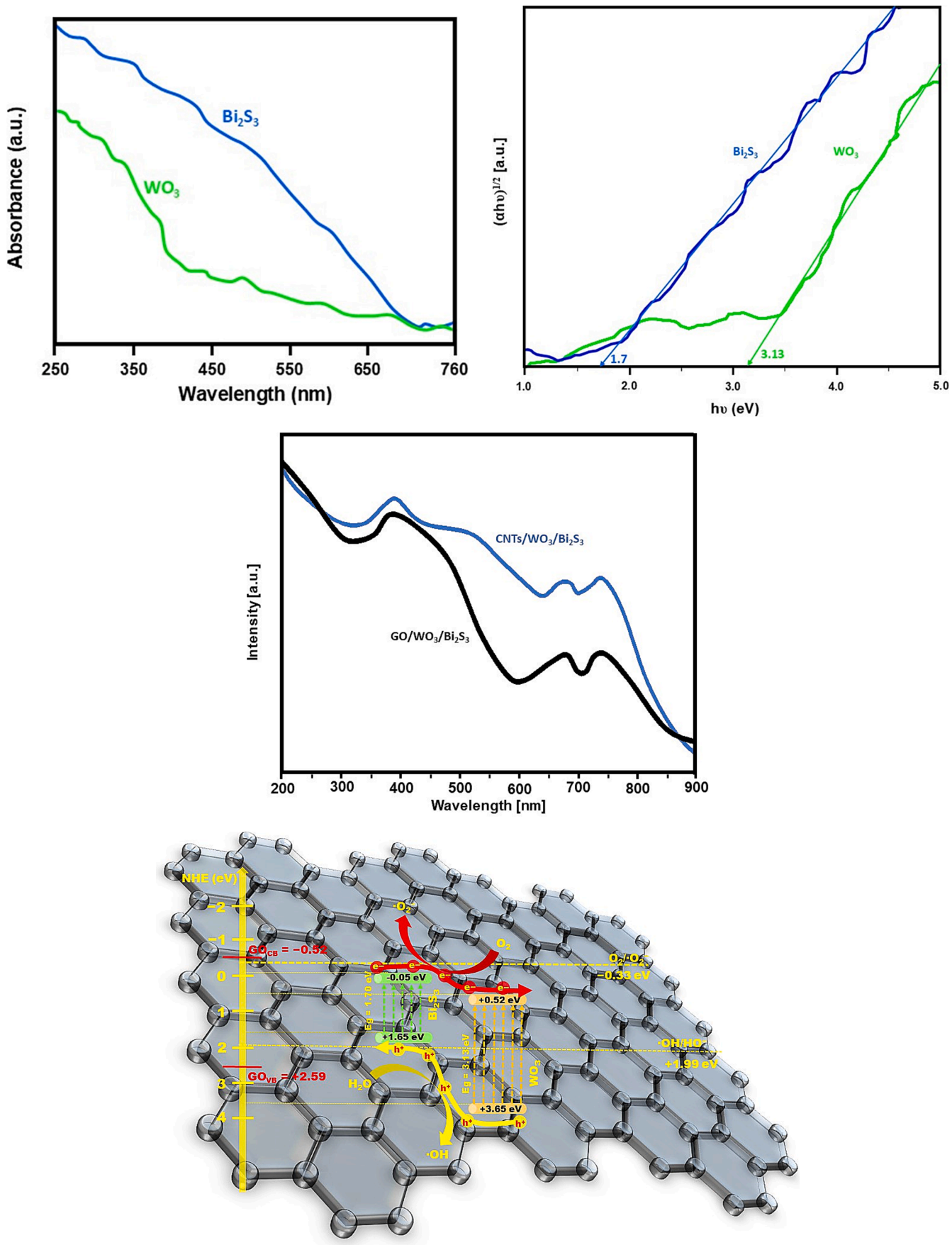

Fig. 12. (a) WO_3 and Bi_2B_3 absorption spectra, (b) WO_3 and Bi_2S_3 Tauc plots, (c) PL spectra, (e) $GO/WO_3/Bi_2S_3$ and (f) $CNTs/WO_3/Bi_2S_3$ band energy diagrams.

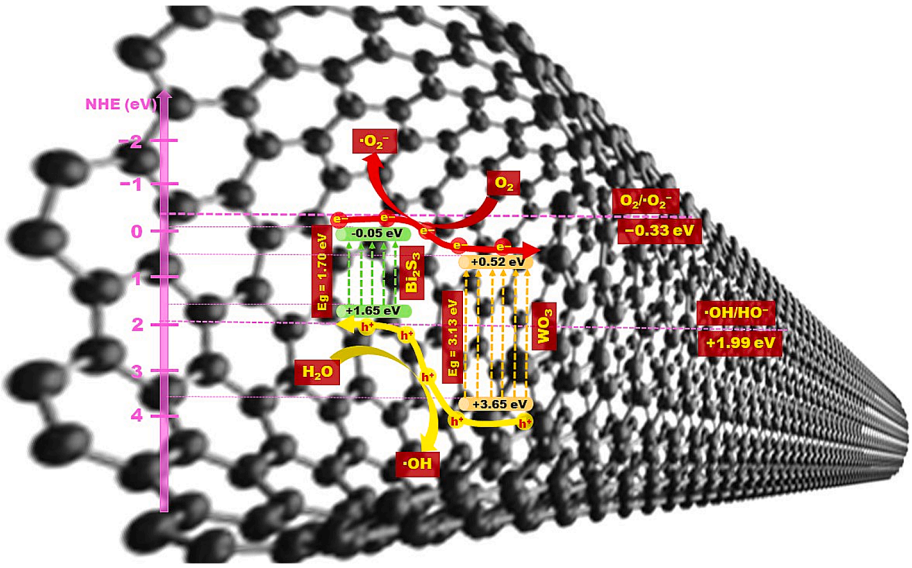

Fig. 12. (*o*).

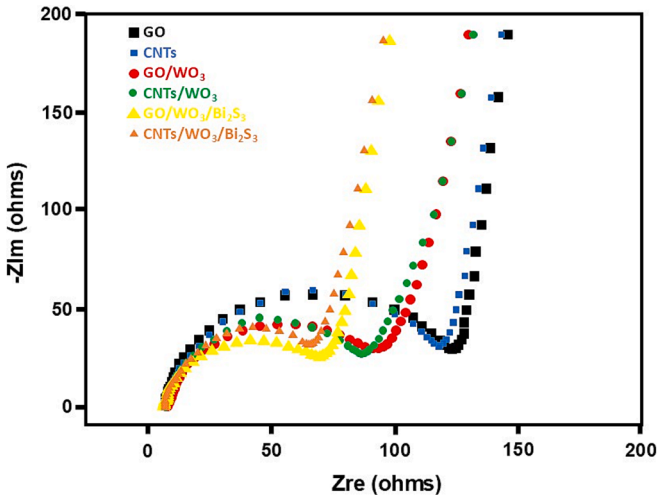

Fig. 13. Electrochemical impedance spectroscopy of the photocatalytic materials.

indicating that junction development will facilitate the charge carriers mobility and decrease the recombination process.

The influence of each ROS (reactive oxidation species) plays a significant role on the photocatalytic removal of PEN-G and AMO. Consequently, the scavenger's experiment was employed to underline the contribution of each oxidative species on the photocatalytic efficiency (see Fig. 14a and b). The scavengers used in this work were: p-BQ (benzoquinone, 0.5 mM) for $\bullet O_2^-$, EDTA (ethylenediaminetetraacetic acid disodium salt, 5 mM) for holes and IPA (isopropyl alcohol, 5 mM) for •OH.

The results presented in Fig. 14 shows that the photocatalytic removal efficiency decreases by 5 % when EDTA is used as scavenger in $CNTs/WO_3/Bi_2S_3$. However, the decrease is significantly higher (12 %) when $GO/WO_3/Bi_2S_3$ is used as photocatalysts. These results indicate that hole's contribution on the photocatalytic process is higher on $GO/WO_3/Bi_2S_3$ compared with $CNTs/WO_3/Bi_2S_3$. When IPA and p-BQ are used as scavengers the photocatalytic activity reduction reach 27 % and 21 %, respectively. The experiments shows that the predominant ROS species that contributed to pollutant removal are •OH and $\bullet O_2^-$.

4. Conclusions

GO and CNTs were involved as template in a simple two-step sol–gel procedure to develop a composite based on $GO/WO_3/Bi_2S_3$ and $CNTs/WO_3/Bi_2S_3$. The samples exhibit crystalline structures corresponding to monoclinic WO_3 and orthorhombic Bi_2S_3. The GO template samples are characterized by a porous sponge-like morphology with 285 m^2/g specific active surface. The CNTs template samples are granular and with slightly higher specific surface (294 m^2/g). EDX measurements indicate that the composite components are uniformly distributed through the sample. Additionally, a deficit of oxygen and sulfur was recorded which may be linked to the synthesis procedure.

The surface energy was tested with two liquids with different polarities and the results indicate that GO template samples have a higher polar component compared with CNTs series. However, for all samples the polar component is significantly higher than dispersive component, which make them suitable for applications in aqueous environment.

The photocatalytic activity was investigated by spectrometry and verified by TOC/TN. Both measurements show similar values which indicate that the pollutant are mineralized. The highest efficiencies correspond to sample $GO/WO_3/Bi_2S_3$ (57.43 % for PEN-G and 63.94 % for AMO) followed by $CNTs/WO_3/Bi_2S_3$. The mechanism evaluation indicates a suitable disposal of the band energy in both composite which increase the concentration of photogenerated charge carriers and decrease the recombination. GO template samples have the advantage of using the CB energy state of GO for additional production of $\bullet O_2^-$ which explain why this sample exhibit better photocatalytic activity. Scavengers experiment indicate that •OH is the dominant ROS used during the photocatalytic degradation of PEN-G and AMO.

Funding

This work was supported by a grant from the Ministry of Research, Innovation and Digitization, CNCS-UEFISCDI, project number PN-III-P4-PCE-2021-1020 (PCE87) within PNCDI III.

Declaration of competing interest

The authors declare that they have no known competing financial interests or personal relationships that could have appeared to influence the work reported in this paper.

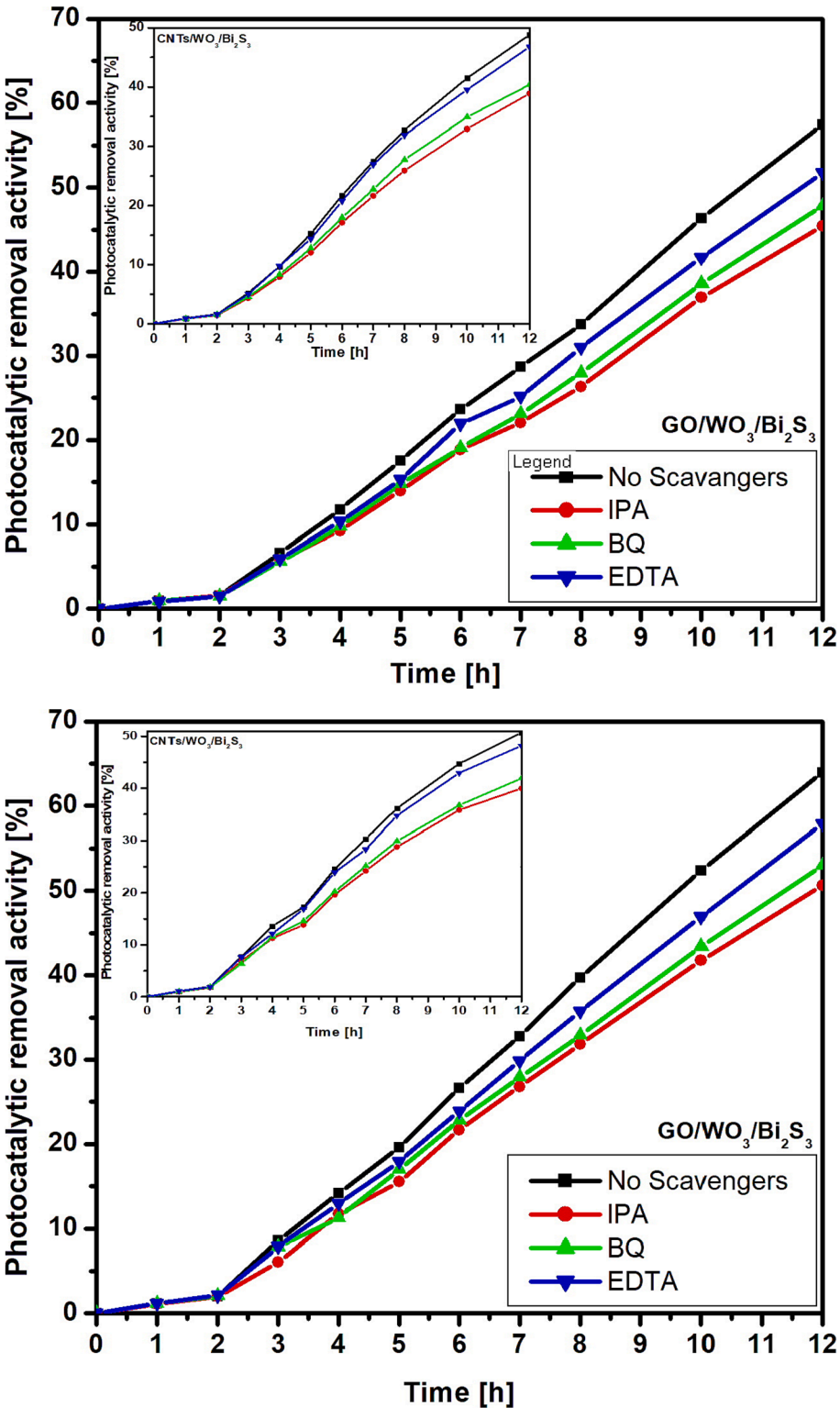

Fig. 14. Scavengers experiments for (a) PEN-G and (b) AMO photocatalytic removal.

Acknowledgments

The author acknowledge the support given by the Tokyo University of Science and Torino University for the experimental investigations.

Data availability

Data will be made available on request.

References

[1] T. Yavuz, K. Clezy, K. Skender, J. Goldberg, F. Vallières, How did the COVID-19 pandemic affect antibiotic consumption within humanitarian emergencies? Results from five humanitarian contexts, Infect. Prev. Pract. 6 (3) (2024) 100385, https://doi.org/10.1016/j.infpip.2024.100385.

[2] X. Yang, X. Li, S. Qiu, C. Liu, S. Chen, H. Xia, Y. Zeng, L. Shi, J. Chen, J. Zheng, S. Yang, G. Tian, G. Liu, L. Yang, Global antimicrobial resistance and antibiotic use in COVID-19 patients within health facilities: A systematic review and meta-

analysis of aggregated participant data, J. Infect. 89 (1) (2024) 106183, https://doi.org/10.1016/j.jinf.2024.106183.
[3] F. Bellanti, A. Lo Buglio, A. Ricci, A. Aquilino, A. Labbate, G. Vendemiale, In-hospital use of antibiotics in internal medicine: A cross-sectional study before, during and after the COVID-19 pandemic in a COVID-19-free ward, J. Infect. Public Health 17 (8) (2024) 102490, https://doi.org/10.1016/j.jiph.2024.102490.
[4] P. Ormaniec, J. Mikosz, Circulation of microplastics in a municipal wastewater treatment plant with multiphase activated sludge, Desal. Water Treat. 317 (2024) 100265, https://doi.org/10.1016/j.dwt.2024.100265.
[5] Z. Li, J. Lu, J. Lu, Energy efficiency evaluation and optimization for wastewater treatment plant, Desal. Water Treat. 319 (2024) 100487, https://doi.org/10.1016/j.dwt.2024.100487.
[6] A. Duta, L. Andronic, A. Enesca, The influence of low irradiance and electrolytes on the mineralization efficiency of organic pollutants using the Vis-active photocatalytic tandem $CuInS_2/TiO_2/SnO_2$, Catal. Today 300 (2018) 18–27, https://doi.org/10.1016/j.cattod.2017.03.018.
[7] A. Markowska-Szczupak, O. Paszkiewicz, K. Yoshiiri, K. Wang, E. Kowalska, Can photocatalysis help in the fight against COVID-19 pandemic? Curr. Opin. Green Sustain. Chem. 40 (2023) 100769 https://doi.org/10.1016/j.cogsc.2023.100769.
[8] J. Lin, H. Hu, N. Gao, J. Ye, Y. Chen, H. Ou, Fabrication of GO@MIL-101(Fe) for enhanced visible-light photocatalysis degradation of organophosphorus contaminant, J. Water Proces. Eng. 33 (2020) 101010, https://doi.org/10.1016/j.jwpe.2019.101010.
[9] S. Yuan, Z. Liu, X. Duan, X. Ren, X. Zhao, Enhancing degradation of sulfamethoxazole by layered double hydroxide/carbon nanotubes catalyst via synergistic effect of photocatalysis/persulfate activation, Environ. Res. 261 (2024) 119647, https://doi.org/10.1016/j.envres.2024.119647.
[10] X. Wang, G. Yang, G. Chai, M.S. Nasir, S. Wang, X. Zheng, C. Wang, W. Yan, Fabrication of heterostructured UIO-66-NH_2/CNTs with enhanced activity and selectivity over photocatalytic CO_2 reduction, Int. J. Hydrogen Energy 45 (2020) 30634–30646, https://doi.org/10.1016/j.ijhydene.2020.08.273.
[11] Y. Yang, D. Zhao, Z. Zhang, Z. Cao, T. Shen, Z. Gu, Y. Miao, Y. Huo, C_3N_4/GO@MF composites for synergistic Adsorption-Photocatalysis contributions to organic pollutant removal, J. Photochem. Photobiol. A 441 (2023) 114729, https://doi.org/10.1016/j.jphotochem.2023.114729.
[12] R. Yu, Y. Yang, L. Tian, X. Li, C. Liu, T. Sun, H. Chang, Z. Zhou, Revealing the membrane fouling behavior and interfacial interaction mechanism in a combined visible light photocatalysis-ultrafiltration system for advanced purification of NOM, J. Water Process Eng. 57 (2024) 104723, https://doi.org/10.1016/j.jwpe.2023.104723.
[13] A. Enesca, A. Duta, Tailoring WO_3 thin layers using spray pyrolysis technique, Phys. Status Solidi C 5 (11) (2008) 3499–3502, https://doi.org/10.1002/pssc.200779410.
[14] A. Mohamed, H. Mahanna, M. Samy, Synergistic effects of photocatalysis-periodate activation system for the degradation of emerging pollutants using GO/MgO nanohybrid, J. Environ. Chem. Eng. 12 (2) (2024) 112248, https://doi.org/10.1016/j.jece:2024.112248.
[15] D. Liu, M. Chen, Y. Han, C. Sun, L. Xu, D. Su, Enhanced directional charge transfer by 2D MXene/Bi_2WO_6/GO in visible light photocatalysis coupled persulfate approach for organic pollutants degradation, Sep. Purif. Technol. 345 (2024) 127328, https://doi.org/10.1016/j.seppur.2024.127328.
[16] F.J.R. Pesqueira, M.R. Pereira, A.M.T. Silva, Carbon-based composites in advanced wastewater treatment: a life cycle assessment of TiO_2 and GO-TiO_2 solar photocatalysis, J. Cleaner Prod. 444 (2024) 140845, https://doi.org/10.1016/j.jclepro.2024.140845.
[17] H. Esfandian, S. Mirzaei, A.S. Chari, R.A. Ghadi, I.H. Moqadam, Photocatalytic degradation of chlorpyrifos pesticide in aqueous solution using Cu-doped TiO_2/GO photocatalysis vicinity of UV and visible light, Mater. Sci. Eng. B 305 (2024) 117385, https://doi.org/10.1016/j.mseb.2024.117385.
[18] S. Yang, Z. Wang, P. Li, X. Wang, L. Li, C.G. Yoo, G. Yang, J. Chen, G. Lyu, Developing of Cu_xSnSO@GO aerogels used as highly efficient catalysts for cellulose transform to lactic acid under the synergy of Cu-Sn thermocatalysis and photocatalysis processes, Chem. Eng. J. 474 (2023) 145716, https://doi.org/10.1016/j.cej.2023.145716.
[19] J.M.P. Silva, N.F. Andrade Neto, A.B. Lima, M. Correa, M.R.D. Bomio, F.V. Motta, Investigating adsorption/photocatalysis of organic contaminants by Fe_3O_4–GO, Fe_3O_4–C_3N_4, and Fe_3O_4–GO-C_3N_4 heterojunctions, Chem. Inorg. Mater. 1 (2023) 100014, https://doi.org/10.1016/j.cinorg.2023.100014.
[20] M. Ali Abbasi, K.M. Amin, M. Ali, Z. Ali, M. Atif, W. Ensinger, W. Khalid, Synergetic effect of adsorption-photocatalysis by GO-CeO_2 nanocomposites for photodegradation of doxorubicin, J. Environ. Chem. Eng. 10 (1) (2022) 107078, https://doi.org/10.1016/j.jece:2021.107078.
[21] S. Li, W. Ji, L. Zou, L. Li, Y. Li, X. Cheng, Crystalline TiO_2 shell microcapsules modified by Co_3O_4/GO nanocomposites for thermal energy storage and photocatalysis, Mater. Today Sustain. 19 (2022) 100197, https://doi.org/10.1016/j.mtsust.2022.100197.
[22] P. Busarello, S. de Quadros, L.M. Zimmermann, E.G.C. Neiva, Graphene oxide/ZnO nanocomposites applied in photocatalysis of dyes: Tailoring aqueous stability of quantum dots, Colloids Surf. A 675 (2023) 132026, https://doi.org/10.1016/j.colsurfa.2023.132026.
[23] M. Zerouali, D. Bouras, R. Daïra, M. Fellah, B. Boudjema, R. Barille, E.F. Sakher, S. Bellucci, G.A. El-Hiti, Effect of Zn-doped CuO thin films on structural, morphological, optical, and electrical properties for photocatalysis application, Opt. Mater. 152 (2024) 115495, https://doi.org/10.1016/j.optmat.2024.115495.
[24] Z. Jia, Y. Yang, C. Yang, D. Wang, Magnetic γ-Fe_2O_3/ZnO@CNTs synthesized by a green precipitation method for the degradation of aniline through photocatalysis coupling catalytic ozonation, Appl. Surf. Sci. 659 (2024) 159866, https://doi.org/10.1016/j.apsusc.2024.159866.
[25] M. Samadi, S. Yousefzadeh, H.S.T. Larijani, K. Rahimi, A. Moshfegh, The superiority of CNT over graphene in $BiVO_4$ nanocomposites for visible light photocatalysis, Opt. Mater. 153 (2024) 115611, https://doi.org/10.1016/j.optmat.2024.115611.
[26] L. Ma, A. Chen, J. Lu, Z. Zhang, H. He, C. Li, In situ synthesis of CNTs/Fe–Ni/TiO_2 nanocomposite by fluidized bed chemical vapor deposition and the synergistic effect in photocatalysis, Particuology 14 (2014) 24–32, https://doi.org/10.1016/j.partic.2013.04.002.
[27] L.W. Zhu, L.K. Zhou, H.X. Li, H.F. Wang, J.P. Lang, One-pot growth of free-standing CNTs/TiO_2 nanofiber membrane for enhanced photocatalysis, Mater. Lett. 95 (2013) 13–16, https://doi.org/10.1016/j.matlet.2013.01.004.
[28] W. Zhang, X. Zhao, Q. Liu, M. Zhang, N. Xi, C. Cui, X. Yu, X. Wang, Y. Wang, H. Liu, Y. Sang, Spontaneous and passive photoinduced charge carrier separation in CNT-$ZnIn_2S_4$ network composites under a magnetic field, Nano Energy 116 (2023) 108806, https://doi.org/10.1016/j.nanoen.2023.108806.
[29] K.M.S. Katubi, S. Akbar, A. Habib, Z.A. Alrowaili, M.S. Al-Buriahi, A. Irshad, M. F. Warsi, Fabrication of CNTs supported $CuCo_2O_4/Co_3S_4$ composite for advanced photocatalytic application, Optik 300 (2024) 171653, https://doi.org/10.1016/j.ijleo.2024.171653.
[30] M.F. Warsi, A. Ihsan, F.M.A. Alzahrani, M.H. Tariq, Z.A. Alrowaili, M.S. Al-Buriahi, M. Shahid, A cost-effective strategy to synthesize perovskite holmium doped $LaFeO_3$ and its composite with CNTs for wastewater treatment, Mater. Sci. Eng. B 301 (2024) 117181, https://doi.org/10.1016/j.mseb.2024.117181.
[31] H.P. Nguyen, T.M. Cao, T.T. Nguyen, V.V. Pham, Improving photocatalytic oxidation of semiconductor (TiO_2, SnO_2, ZnO)/CNTs for NO_x removal, J. Ind. Eng. Chem. 127 (2023) 321–330, https://doi.org/10.1016/j.jiec.2023.07.017.
[32] H. Yu, B. Ji, D. Wang, Synthesis of Cu-WO_3-CNT nanocomposite and its electrochemical and photocatalytic properties: application for Cr(VI) removal from aqueous solution, Int. J. Electrochem. Sci. 18 (9) (2023) 100247, https://doi.org/10.1016/j.ijoes.2023.100247.
[33] D. Fan, M. Hu, S. Li, P. Chen, H. Jiang, X. Tu, X. Li, X. Luo, CNTs with nano-confined TiO_2 and surface loading Co_3O_4: the analysis of its performance and mechanism of PMS activation for ECs degradation under visible light, Sep. Purif. Technol. 352 (2025) 127840, https://doi.org/10.1016/j.seppur.2024.127840.
[34] E. Petrus, M. Segado, C. Bo, Nucleation mechanisms and speciation of metal oxide clusters, Chem. Sci. 11 (32) (2020) 8448–8456, https://doi.org/10.1039/d0sc03530k.
[35] A. Enesca, L. Andronic, A. Duta, S. Manolache, Optical properties and chemical stability of WO_3 and TiO_2 thin films photocatalysts, Roman. J. Inf. Sci. Technol. 10 (3) (2007) 269–277.
[36] F. Chen, S. Li, Q. Chen, X. Zheng, P. Liu, S. Fang, 3D graphene aerogels-supported Ag and Ag@Ag_3PO_4 heterostructure for the efficient adsorption-photocatalysis capture of different dye pollutants in water, Mater. Res. Bull. 105 (2018) 334–341, https://doi.org/10.1016/j.materresbull.2018.05.013.
[37] X. Li, W. Zhang, W. Cui, Y. Sun, G. Jiang, Y. Zhang, H. Huang, F. Dong, Bismuth spheres assembled on graphene oxide: Directional charge transfer enhances plasmonic photocatalysis and in situ DRIFTS studies, Appl. Catal. B 221 (2018) 482–489, https://doi.org/10.1016/j.apcatb.2017.09.046.
[38] T.T. Pham, E.W. Shin, Thermal formation effect of g-C_3N_4 structure on the visible light driven photocatalysis of g-C_3N_4/$NiTiO_3$ Z-scheme composite photocatalysts, Appl. Surf. Sci. 447 (2018) 757–766, https://doi.org/10.1016/j.apsusc.2018.04.051.
[39] V.D.B.C. Dasireddy, B. Likozar, Selective photocatalytic oxidation of benzene to phenol using carbon nanotube (CNT)-supported Cu and TiO_2 heterogeneous catalysts, J. Taiwan Inst. Chem. Eng. 82 (2018) 331–341, https://doi.org/10.1016/j.jtice:2017.11.011.
[40] S. Ozbay, N. Erdogan, F. Erden, M. Ekmekcioglu, M. Ozdemir, G. Aygun, L. Ozyuzer, Surface free energy analysis of ITO/Au/ITO multilayer thin films on polycarbonate substrate by apparent contact angle measurements, Appl. Surf. Sci. 529 (2020) 147111, https://doi.org/10.1016/j.apsusc.2020.147111.
[41] S. Rbihi, A. Aboulouard, L. Laallam, A. Jouaiti, Contact Angle measurements of cellulose based thin film composites: wettability, surface free energy and surface hardness, Surf. Interface 21 (2020) 100708, https://doi.org/10.1016/j.surfin.2020.100708.
[42] L. Tachon, S. Guignard, An accurate optical method for the measurement of contact angle and interface shape of evaporative thin liquids films, Exp. Therm. Fluid Sci. 90 (2018) 66–75, https://doi.org/10.1016/j.expthermflusci.2017.08.011.
[43] J.M. Ribeiro, F.C. Correia, P.B. Salvador, L. Rebouta, L.C. Alves, E. Alves, N. P. Barradas, A. Mendes, C.J. Tavares, Compositional analysis by RBS, XPS and EDX of ZnO:Al,Bi and ZnO:Ga,Bi thin films deposited by d.c. magnetron sputtering, Vacuum 161 (2019) 268–275, https://doi.org/10.1016/j.vacuum.2018.12.038.
[44] B. Thomas, B. Skariah, Spray deposited Mg-doped SnO_2 thin film LPG sensor: XPS and EDX analysis in relation to deposition temperature and doping, J. Alloys Compound. 625 (2015) 231–240, https://doi.org/10.1016/j.jallcom.2014.11.092.
[45] K.I. Dragnevski, A.M. Donald, S.M. Clarke, A. Maltby, Novel applications of ESEM and EDX for the study of molecularly thin amide monolayers on polymer films, Colloids Surf. A 337 (1–3) (2009) 47–51, https://doi.org/10.1016/j.colsurfa.2008.11.039.
[46] S. Erat, H. Metin, M. Arı, Influence of the annealing in nitrogen atmosphere on the XRD, EDX, SEM and electrical properties of chemical bath deposited CdSe thin films, Mater. Chem. Phys. 111 (1) (2008) 114–120, https://doi.org/10.1016/j.matchemphys.2008.03.021.

[47] A. Enesca, V. Sisman, UV-Vis activated CuO/CuS/WO_3@PANI heterostructure for photocatalytic removal of pharmaceutical active compounds, Ceram. Int. 49 (21) (2023) 30592–30602, https://doi.org/10.1016/j.ceramint.2023.07.012.
[48] W. Thomas, B. Krishnan, D.A. Avellaneda, E.O.G. Sanchez, J.A.A. Martinez, S. Shaji, Defects induced SnO_x-TiO_2 nanocomposite thin films for improved visible light driven photocatalysis and photoelectrochemical applications, Appl. Surf. Sci. 669 (2024) 160575, https://doi.org/10.1016/j.apsusc.2024.160575.
[49] J. Singh, R.K. Soni, Fabrication of nanostructured In_2S_3 thin film with broad optical absorption for improved sunlight mediated photocatalysis application, Opt. Mater. 122 (2021) 111748, https://doi.org/10.1016/j.optmat.2021.111748.
[50] A. Karuppasamy, Enhanced photocatalysis and photohydrophilicity in TiO_2–W_5O_{14} nanocomposite thin films grown by in-lay sputtering, Mater. Chem. Phys. 301 (2023) 127580, https://doi.org/10.1016/j.matchemphys.2023.127580.
[51] M. Castañeda-Juárez, V. Martínez-Miranda, P.T. Almazán-Sánchez, I. Linares-Hernández, F. Santoyo-Tepole, G. Vázquez-Mejía, Synthesis of TiO_2 catalysts doped with Cu, Fe, and Fe/Cu supported on clinoptilolite zeolite by an electrochemical-thermal method for the degradation of diclofenac by heterogeneous photocatalysis, J. Photochem. Photobiol. A 380 (2019) 111834, https://doi.org/10.1016/j.jphotochem.2019.04.045.
[52] M. Antonopoulou, C. Kosma, T. Albanis, I. Konstantinou, An overview of homogeneous and heterogeneous photocatalysis applications for the removal of pharmaceutical compounds from real or synthetic hospital wastewaters under lab or pilot scale, Sci. Total Environ. 765 (2021) 144163, https://doi.org/10.1016/j.scitotenv.2020.144163.
[53] M.Z. Fidelis, Y.B. Favaro, A.S.G.G. dos Santos, M.F.R. Pereira, R. Brackmann, G. G. Lenzi, O.S.G.P. Soares, O.A.B. Andreo, Enhancing ibuprofen and 4-isobutylacetophenone degradation: exploiting the potential of Nb_2O_5 sol-gel catalysts in photocatalysis, catalytic ozonation, and photocatalytic ozonation, J. Environ. Chem. Eng. 11 (5) (2023) 110690, https://doi.org/10.1016/j.jece:2023.110690.
[54] K. Stando, P. Zogornik, M. Kopiec, M. Pieszczek, K. Kowalska, E. Felis, S. Bajkacz, Degradation of fluoroquinolones and macrolides by solar light-driven heterogeneous photocatalysis – Proposed drug transformation pathways, J. Photochem. Photobiol. A 453 (2024) 115651, https://doi.org/10.1016/j.jphotochem.2024.115651.
[55] R.M.B. Ramos, L.C. Paludo, P.I. Monteiro, L.V.M. da Rocha, C.V. de Moraes, O. O. Santos, E.R. Alves, T.L.P. Dantas, Amoxicillin degradation by iron photonanocatalyst synthetized by green route using pumpkin (Tetsukabuto) peel extract, Talanta 260 (2023) 124658, https://doi.org/10.1016/j.talanta.2023.124658.
[56] A. Fawzy, H. Mahanna, M. Mossad, Effective photocatalytic degradation of amoxicillin using MIL-53(Al)ZnO composite, Environ. Sci. Pollut. Control Ser. 29 (2022) 68532–68546, https://doi.org/10.1007/s11356-022-20527-0.
[57] D.T. Lalliansanga, S.-M. Lee, D.-J. Kim, Photocatalytic degradation of amoxicillin and tetracycline by template synthesized nano-structured Ce3+@TiO thin film catalyst, Environ. Res. 210 (2022) 112914, https://doi.org/10.1016/j.envres.2022.112914.
[58] A. Enesca, L. Andronic, A. Duta, The influence of surfactants on the crystalline structure, electrical and photocatalytic properties of hybrid multi-structured (SnO_2, TiO_2 and WO_3) thin films, Appl. Surf. Sci. 258 (10) (2016) 4339–4346, https://doi.org/10.1016/j.apsusc.2011.12.110.
[59] M. Nami, S. Sheibani, F. Rashchi, Photocatalytic performance of coupled semiconductor ZnO–CuO nanocomposite coating prepared by a facile brass anodization process, Mater. Sci. Semiconductor Process. 135 (2021) 106083, https://doi.org/10.1016/j.mssp.2021.106083.
[60] C. Gao, J. Li, Z. Shan, F. Huang, H. Shen, Preparation and visible-light photocatalytic activity of In_2S_3/TiO_2 composite, Mater. Chem. Phys. 122 (2010) 183–187, https://doi.org/10.1016/j.matchemphys.2010.02.030.
[61] T. Mise, T. Nakada, Low temperature growth and properties of Cu–In–Te based 433 thin films for narrow bandgap solar cells, Thin Solid Films 518 (2010) 5604–5609, https://doi.org/10.1016/j.tsf.2010.04.065.
[62] J. Malik, S. Kumar, T.K. Mandal, Reactive species specific RhB assisted collective photocatalytic degradation of tetracycline antibiotics with triple-layer Aurivillius perovskites, Catal. Sci. Technol. 12 (2022) 6704–6716, https://doi.org/10.1039/D1CY01644J.
[63] X. Guo, J. Duan, C. Li, Z. Zhang, W. Wang, Highly efficient Z-scheme g-C_3N_4/ZnO photocatalysts constructed by co-melting-recrystallizing mixed precursors for wastewater treatment, J. Mater. Sci. 55 (2020) 2018–2031, https://doi.org/10.1007/s10853-019-04097-0.